

**Frequency conversion by nonlinear optics:
narrow bandwidth sources and applications**

VRIJE UNIVERSITEIT

**Frequency conversion by nonlinear optics:
narrow bandwidth sources and applications**

ACADEMISCH PROEFSCHRIFT

ter verkrijging van de graad van doctor aan
de Vrije Universiteit Amsterdam,
op gezag van de rector magnificus
prof.dr. T. Sminia,
in het openbaar te verdedigen
ten overstaan van de promotiecommissie
van de faculteit der Exacte Wetenschappen
op dinsdag 2 december 2003 om 13.45 uur
in de aula van de universiteit,
De Boelelaan 1105

door

Joop Mes

geboren te Bergen op Zoom

promotor: prof.dr. W. Hogervorst
copromotoren: dr. J.C. van den Heuvel
 dr. E.J. van Duijn

The work described in this thesis was performed with financial support of "TNO fysisch elektronisch lab" (TNO-FEL), and was carried out at the Laser Centre of the Vrije Universiteit Amsterdam.

"Kennis is nog geen wijsheid"

Arthur Schopenhauer

Contents

| | | |
|----------|--|-----------|
| 1 | Nonlinear optics: optical parametric oscillators and other applications | 1 |
| 1.1 | Introduction | 1 |
| 1.2 | Nonlinear processes | 3 |
| 1.2.1 | Linear polarization | 3 |
| 1.2.2 | Anisotropy | 7 |
| 1.2.3 | Nonlinear effects | 8 |
| 1.2.4 | Anharmonic oscillator | 10 |
| 1.3 | Crystals | 10 |
| 1.3.1 | Phase matching | 11 |
| 1.3.2 | Walk-off | 13 |
| 1.4 | Optical parametric oscillators | 15 |
| 1.4.1 | Fourier-transform-limited pulses | 15 |
| 1.4.2 | Grazing incidence cavity | 16 |
| 1.4.3 | Relay imaging | 18 |
| 1.4.4 | Spectrum analyser | 20 |
| 1.5 | Continuous wave frequency mixing | 24 |
| 1.6 | Enhancement cavities | 24 |
| 1.6.1 | Mode matching | 26 |
| 1.6.2 | Hänsch-Couillaud locking scheme | 28 |
| 2 | A SLM optical parametric oscillator for spectroscopic applications | 33 |
| 2.1 | Abstract | 33 |
| 2.2 | Introduction | 33 |
| 2.3 | Experimental setup | 34 |
| 2.4 | Applications | 38 |
| 2.5 | Conclusion | 40 |
| 3 | Travelling-wave nanosecond Optical Parametric Oscillator close to the Fourier-transform limit | 41 |
| 3.1 | Abstract | 41 |
| 3.2 | Introduction | 41 |
| 3.3 | Experimental setup | 43 |

| | | |
|----------|--|-----------|
| 3.4 | Results | 45 |
| 3.5 | Discussion | 48 |
| 3.6 | Conclusion | 50 |
| 4 | Third-harmonic generation of a cw Ti:Sapphire laser in external resonant cavities | 53 |
| 4.1 | Introduction | 53 |
| 4.2 | Experimental setup | 54 |
| 4.3 | Conclusion | 59 |
| 5 | High-resolution spectroscopy on ground-state transitions of samarium-I | 61 |
| 5.1 | Introduction | 61 |
| 5.2 | Experimental setup | 62 |
| 5.3 | Measurements | 65 |
| 5.3.1 | hyperfine structure | 65 |
| 5.3.2 | Isotope splitting | 68 |
| 5.4 | Discussion | 71 |
| 5.5 | Conclusion | 73 |
| | Summary | 75 |
| | Samenvatting | 78 |
| | Dankwoord | 82 |

Chapter 1

Nonlinear optics: optical parametric oscillators and other applications

1.1 Introduction

Optical parametric oscillators (OPO) and frequency mixing devices are (solid-state) sources of coherent radiation that can be used to extend the wavelength range of existing lasers. Such sources are the subject of investigation in this work. In general, they consist of a nonlinear medium inside an optical resonator. In the nonlinear medium a three-wave interaction takes place. In an OPO (see fig. 1.1) an incident laser beam (the pump) is converted into two new wavelengths (the signal and idler beam) while conserving energy,

$$\omega_{pump} = \omega_{signal} + \omega_{idler}, \quad (1.1)$$

and momentum

$$\vec{k}_{pump} = \vec{k}_{signal} + \vec{k}_{idler}, \quad (1.2)$$

where \vec{k}_i is the wave vector corresponding to the frequency ω_i

$$\vec{k}_i = 2\pi \frac{n_i}{\lambda_i}, \quad (1.3)$$

Here n_i the refractive index and λ_i the wavelength.

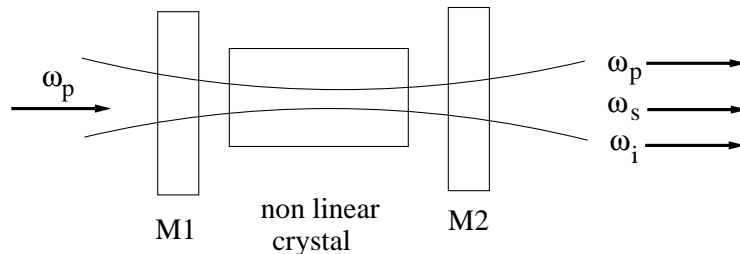


Figure 1.1: Optical parametric oscillator; the mirror $M1$ is highly reflective for the signal wave ω_s or/and idler wave ω_i , highly transparent for the pump wavelength ω_p . The output coupler $M2$ is partially reflecting ω_s or/and ω_i and highly transparent for ω_p .

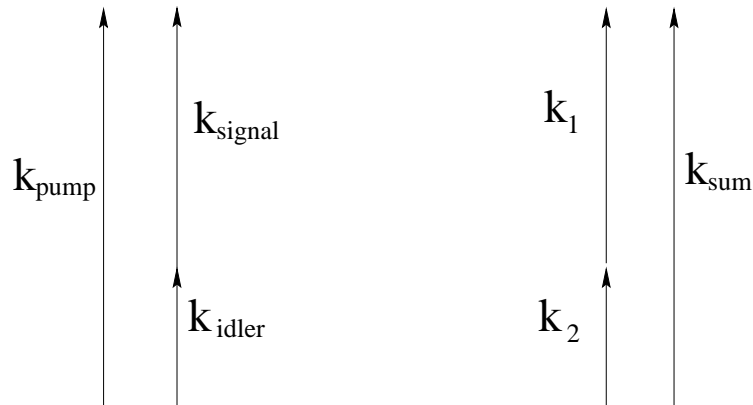


Figure 1.2: *Left: One high-energy photon is split into two photons of lower energy: Optical parametric generation. Right: Sum-frequency mixing: Two low-energy photons (k_1 and k_2) are added to generate a high-energy photon.*

Frequency mixing can be considered to be the opposite process of optical parametric generation (see fig. 1.2); two wavelengths are combined in a nonlinear medium to generate the sum or the difference of the frequencies of the incident waves, again conserving momentum and energy. The above relations now become

$$\omega_{in1} + \omega_{in2} = \omega_{out}, \quad (1.4)$$

$$\vec{k}_{in1} + \vec{k}_{in2} = \vec{k}_{out}, \quad (1.5)$$

for sum frequency mixing. By "adding up" two visible photons, higher energy photons can be generated, *e.g.*, sum-frequency mixing can be used to generate ultra-violet light. Difference frequency mixing can be used to produce coherent infra-red light, as low energy photons are generated. These techniques can be applied to generate coherent light in a broad range of wavelengths in the electro-magnetic spectrum. Up to now, most tunable (narrow-bandwidth) laser sources are dye lasers, which have several disadvantages. Laser dyes are usually harmful for health, they have a limited lifetime and produce chemical waste. Therefore, these lasers are not considered to be very user friendly. Solid state lasers in combination with nonlinear techniques do not have these disadvantages, moreover, radiation in an extended wavelength range, starting from 200 nm up to 5 μm can be generated nowadays.

Development of solid state laser devices is of great importance. The challenge in this field is the ability to control the output characteristics of the generated coherent radiation, such as wavelength, pulse length and bandwidth. For spectroscopic and many other applications often a narrow-bandwidth is desirable. This thesiswork is focused on generation of narrow-bandwidth radiation by both pulsed and continuous wave devices.

1.2 Nonlinear processes

In this section the background of nonlinear interactions in a medium is summarised. First linear polarization is described and it is shown how this can be used as a source term in the Maxwell equations. Next, the nonlinear polarization is treated and it is shown how new EM-fields can be generated. Text-books by Zernike et al. [2], Shen [3] and Yariv [4] can be used for further reading.

1.2.1 Linear polarization

Nonlinear optical devices are based on the nonlinear response of the dielectric material polarization to an applied strong electro-magnetic field (see fig. 1.3 and 1.4). The dielectric material polarization P is defined as the induced dipole moment per unit volume. According to the classical model of Lorentz, a material will be polarized, as a response to an applied electro-magnetic (EM) field i.e., electrons are affected by external electric forces that displace them. The motion of the electrons is restored by the binding force. The electronic dipoles will oscillate in tune with the oscillation of the applied EM field. This movement can be described by the equation of motion of a damped harmonic oscillator,

$$\frac{d^2r}{dt^2} + 2\gamma \frac{dr}{dt} + \omega_0^2 r = -\frac{e}{m} E. \quad (1.6)$$

Here r is the displacement of the electron from its equilibrium position, e is the electron charge, m the electron mass, ω_0 is the resonance frequency, γ is a damping constant and E is the applied electric field. The electric field in complex notation can be expressed as:

$$E(t) = E(\omega)e^{-i\omega t} + E^*(\omega)e^{+i\omega t} \quad (1.7)$$

where $E(\omega)$ is a complex amplitude that includes a phase

$$E(\omega) = \frac{1}{2}\varepsilon e^{i\phi} \quad (1.8)$$

and $E^*(\omega)$ is the complex conjugate of $E(\omega)$. Substituting this field in eq. 1.6 leads to the following solution for the motion of a single electron:

$$r = -\frac{e}{m} E(\omega) \frac{e^{-i\omega t}}{\omega_0^2 - 2i\gamma\omega - \omega^2} + c.c.. \quad (1.9)$$

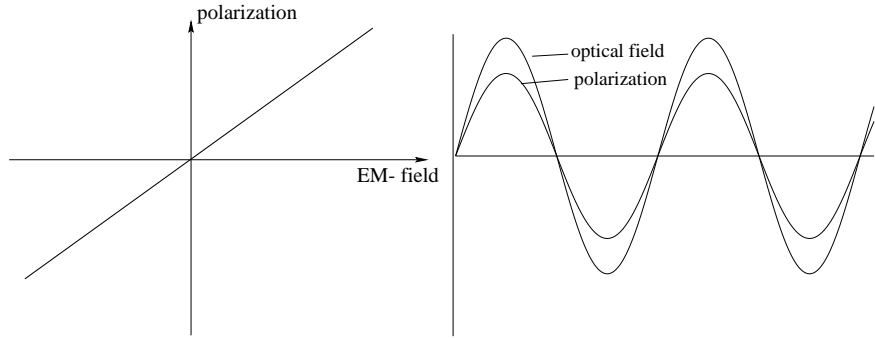


Figure 1.3: *Linear response of the polarization on an applied E-M field.*

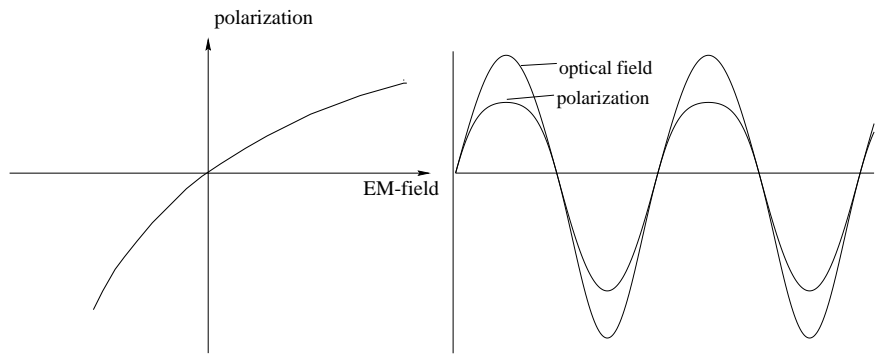


Figure 1.4: *Nonlinear response of the polarization on an applied EM field. When Fourier-transformation is applied to the polarization wave, it is seen that the generated EM wave contains higher harmonics.*

In a medium with electron density N a polarization density $P = -Ner$ can be defined. This polarization density then becomes:

$$P = -\frac{Ne^2}{m} \frac{E(\omega)e^{-i\omega t}}{\omega_0^2 - 2i\gamma\omega - \omega^2} + c.c., \quad (1.10)$$

where c.c. is the complex conjugate. The susceptibility $\chi(\omega)$ can be introduced as:

$$\chi(\omega) = -\frac{Ne^2}{m} \frac{1}{\omega_0^2 - 2i\gamma\omega - \omega^2}. \quad (1.11)$$

With this definition the polarization density (eq. 1.10) becomes

$$P = \chi(\omega)E(\omega)e^{-i\omega t} + c.c. \quad (1.12)$$

This simple model shows that the induced polarization is linearly proportional to the applied field and oscillates at the same frequency. The induced polarization will act as a source term for a re-radiated EM field. In the linear case the re-radiated EM field has the

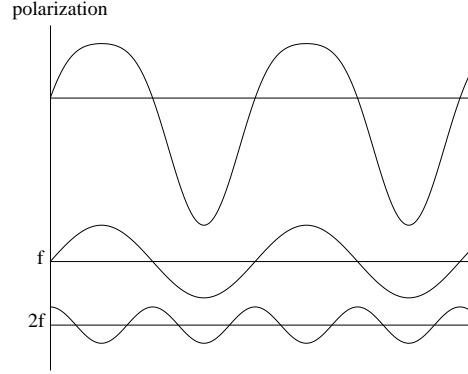


Figure 1.5: The material polarization as depicted in fig. 1.4 can be decomposed into the frequencies f and $2f$.

same frequency as the applied field. This can be shown using the Maxwell equations:

$$\begin{aligned}
 \nabla \times \vec{E} &= -\frac{1}{c} \frac{\partial \vec{B}}{\partial t}, \\
 \nabla \times \vec{H} &= \frac{4\pi}{c} \vec{J} + \frac{1}{c} \frac{\partial \vec{D}}{\partial t}, \\
 \nabla \cdot \vec{D} &= \rho, \\
 \nabla \cdot \vec{B} &= 0,
 \end{aligned} \tag{1.13}$$

and the additional relations, for the dielectric displacement \vec{D} , the magnetic field \vec{B} and the current density \vec{J}

$$\vec{D} = \epsilon \vec{E}, \tag{1.14}$$

$$\vec{B} = \mu \vec{H}, \tag{1.15}$$

$$\vec{J} = \sigma \vec{E}. \tag{1.16}$$

Further $\epsilon = \epsilon_0(1 + 4\pi\chi)$ so eq. 1.14 becomes:

$$\vec{D} = \epsilon_0(1 + 4\pi\chi)\vec{E} = \epsilon_0(\vec{E} + 4\pi\vec{P}). \tag{1.17}$$

Here \vec{D} contains the material polarization $\vec{P} = \chi\vec{E}$, which acts as a source term to generate an EM wave. The polarization field is inserted as a source term. Now eq. 1.13-2 becomes

$$\nabla \times \vec{H} = \frac{4\pi}{c} \sigma \vec{E} + \frac{\epsilon}{c} \frac{\partial \vec{E}}{\partial t}. \tag{1.18}$$

Here σ is the conductivity. Taking the curl of eq. 1.13-1 gives:

$$\nabla \times \nabla \times \vec{E} = -\frac{1}{c} \left(\frac{\partial}{\partial t} \right) \nabla \times \vec{B}. \quad (1.19)$$

Together with eq. 1.15 this gives:

$$\nabla \times \nabla \times \vec{E} = -\frac{1}{c} \left(\frac{\partial}{\partial t} \right) \nabla \times \mu \vec{H}. \quad (1.20)$$

The optical medium is usually non-conducting and non-magnetic, so $\sigma = 0$ and $\mu = 1$. Using the relations $\nabla \times \nabla \times \vec{E} = \nabla \nabla \cdot \vec{E} - \nabla^2 \vec{E}$ and $\nabla \cdot \vec{E} = 0$ and substituting eq 1.18 gives:

$$\nabla \times \nabla \times \vec{E} = -\nabla^2 \vec{E} = -\frac{1}{c} \frac{\partial}{\partial t} \left(\frac{\epsilon}{c} \right) \left(\frac{\partial \vec{E}}{\partial t} \right), \quad (1.21)$$

so:

$$\nabla^2 \vec{E} = \frac{\epsilon}{c^2} \frac{\partial^2}{\partial t^2} \vec{E}. \quad (1.22)$$

Reducing the problem to one dimension (plane wave propagating along the z-axis) eq. 1.22 reduces to:

$$\frac{\partial^2 \vec{E}}{\partial z^2} = \frac{\epsilon}{c^2} \frac{\partial^2}{\partial t^2} \vec{E} \quad (1.23)$$

A possible solution is a travelling wave

$$\vec{E}(z, t) = \epsilon E(\omega) e^{-i(\omega t + kz)} + c.c. \quad (1.24)$$

This gives inserted in eq. 1.23

$$k^2 = \frac{\epsilon \omega^2}{c^2} \quad (1.25)$$

k is the one-dimensional wave-vector $k = \frac{n\omega}{c}$, so $n^2 = \epsilon$ or

$$n^2 = \epsilon_0 (1 + 4\pi\chi) \quad (1.26)$$

Substituted in eq. 1.11 we find

$$n^2 = \epsilon_0 + \frac{Ne^2}{m} \frac{4\pi\epsilon_0}{\omega_0^2 - 2i\gamma\omega - \omega^2}. \quad (1.27)$$

If the material has no damping ($\gamma = 0$) n is a real quantity, if $\gamma \neq 0$, n is complex. The real part is related to the index of refraction n of a medium the imaginary part is related to the absorption coefficient. The behaviour of $n(\omega)$ is plotted in figure 1.6.

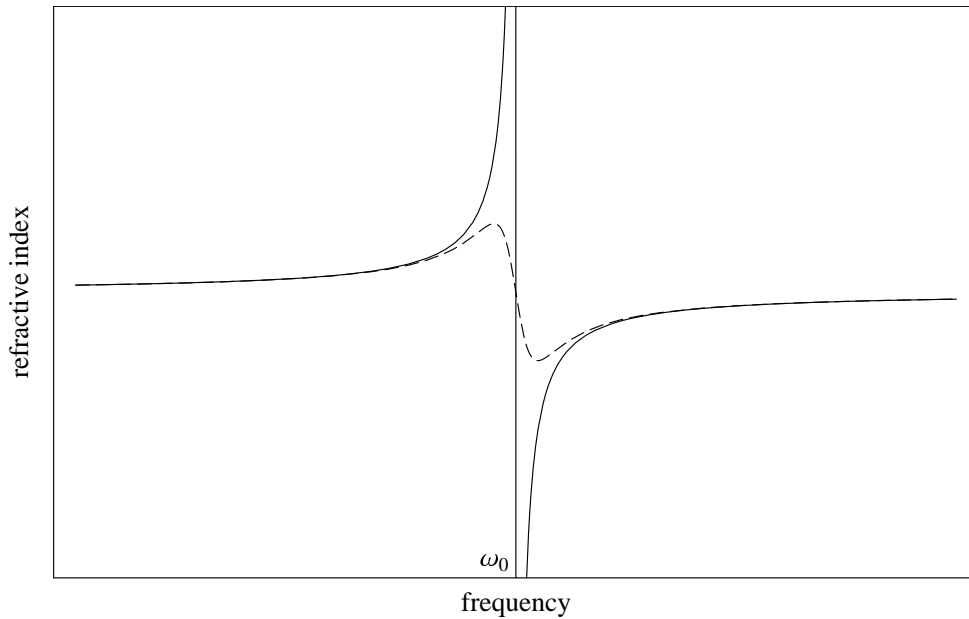


Figure 1.6: *The refractive index n as function of the frequency ω . If the material has no damping $\gamma = 0$, n has a discontinuity at ω_0 (solid line), in case of damping $\gamma \neq 0$ the curve is continuous (dashed line). In practice crystals will always have damping caused by absorption.*

1.2.2 Anisotropy

In figure 1.6 the behaviour of the refractive index of a material modulated by an electromagnetic field with a frequency ω is shown. The natural frequency ω_0 and the refractive index of a material are influenced by the interaction between the atoms constituting the medium. In some materials this interaction is not the same in all directions, these materials are called anisotropic. The dielectric constant D in these anisotropic materials is a second-rank tensor, since it relates the dielectric displacement in one direction to the fields in each of the three directions.

$$D_i = \epsilon_{ij} E_j, \quad (1.28)$$

When using the symmetry of the tensor and a suitable choice of the coordinate axes, the dielectric constant can be written as:

$$\begin{pmatrix} D_x \\ D_y \\ D_z \end{pmatrix} = \begin{pmatrix} \epsilon_x & 0 & 0 \\ 0 & \epsilon_y & 0 \\ 0 & 0 & \epsilon_z \end{pmatrix} \begin{pmatrix} E_x \\ E_y \\ E_z \end{pmatrix} \quad (1.29)$$

Anisotropy can also be induced by an external influence, such as strain or an electrical field. These influences should be large enough to perturb the interatomic fields to a significant extend.

1.2.3 Nonlinear effects

When the refractive index of a crystal is phase modulated by a strong electro-magnetic field of frequency ω_a , then a beam with frequency ω_b which passes through this crystal will also be phase modulated. Side bands at combination frequencies are generated, such as sum frequencies $\omega_{sum} = \omega_a + \omega_b$ and difference frequencies $\omega_{diff} = \omega_a - \omega_b$. Thus different frequencies can be created by modulating the parameters of the crystal. This explains the name optical parametric oscillator.

The nonlinear behaviour of a medium is generally so weak that it can only be exploited when the amplitudes of the applied electromagnetic fields ω_a and ω_b are large: these should be of the same order of magnitude as the interatomic fields. When only one of the interacting fields has a large amplitude, a second weaker field can still be modulated and amplified. In optical parametric oscillators, the modulating field (usually referred to as the "pump" field) has a large amplitude, the other fields are initially non-existing (or at least not detectable). They start from noise in the crystal and are amplified by the pump field.

The interaction of an applied EM field with the medium can result in a nonlinear contribution to the polarization. In case of weak fields, the polarization of a material can be written as (see eq. 1.12):

$$\vec{P} = \chi^{(1)} \vec{E}, \quad (1.30)$$

with the linear susceptibility $\chi^{(1)}$. When the applied field is intense, the electrons will no longer oscillate harmonically and anharmonic terms will appear in the induced polarization of the material. In this case the polarization can be expressed as:

$$\vec{P}_{total} = \chi^{(1)} \vec{E}_1 + \chi^{(2)} \vec{E}^2 + \chi^{(3)} \vec{E}^3 + \dots \quad (1.31)$$

In the non-perturbative regime, the $\chi^{(1)} \vec{E}$ term dominates and the higher order terms can be neglected, since $\chi^{(1)} \vec{E} \gg \chi^{(2)} \vec{E}^2 \gg \chi^{(3)} \vec{E}^3$ and so on. The first nonlinear component of the polarization is

$$\vec{P}_{NL}^{(2)} = \chi^{(2)} \vec{E}^2 = 2d\vec{E}^2. \quad (1.32)$$

Consider *e.g.*, two travelling waves ε_1 and ε_2 :

$$\varepsilon_1(z, t) = \varepsilon_1 \cos(\omega_1 t + k_1 z), \quad (1.33)$$

$$\varepsilon_2(z, t) = \varepsilon_2 \cos(\omega_2 t + k_2 z). \quad (1.34)$$

When substituted in eq. 1.32, their interaction will result in the following nonlinear polarization:

$$\vec{P}_{NL}^{(2)} = 2d[\varepsilon_1^2 \cos(\omega_1 t + k_1 z) + \varepsilon_2^2 \cos(\omega_2 t + k_2 z) + 2\varepsilon_1 \varepsilon_2 \cos(\omega_1 t + k_1 z) \cos(\omega_2 t + k_2 z)]. \quad (1.35)$$

From eq. 1.35 it can be seen that the first order nonlinear polarization contains components with various combination frequencies:

$$\vec{P}_{2\omega_1} = 2d\varepsilon_1^2 \cos 2(\omega_1 t + k_1 z). \quad (1.36)$$

$$\vec{P}_{2\omega_2} = 2d\varepsilon_2^2 \cos 2(\omega_2 t + k_2 z). \quad (1.37)$$

$$\vec{P}_{\omega_1+\omega_2} = 2d\varepsilon_1 \varepsilon_2 \cos((\omega_1 + \omega_2)t + (k_1 + k_2)z). \quad (1.38)$$

$$\vec{P}_{\omega_1-\omega_2} = 2d\varepsilon_1 \varepsilon_2 \cos((\omega_1 - \omega_2)t + (k_1 - k_2)z). \quad (1.39)$$

The second harmonic of both waves (frequency doubling), as well as sum and difference frequency terms result. The nonlinear polarization, inserted as a source term in Maxwell's equations, is responsible for the generation of EM waves at various new combination frequencies (see fig. 1.5).

1.2.4 Anharmonic oscillator

The equation of motion for an anharmonic oscillator describes the nonlinearity in the polarization,

$$\frac{d^2r}{dt^2} + 2\gamma\frac{dr}{dt} + \omega_0^2r - \mu r^2 = -\frac{e}{m}E. \quad (1.40)$$

Equation 1.40 does not have a simple exact solution because of the anharmonic term (μr^2). The anharmonic contribution is usually small, so a solution in the form of a power series

$$r_i = a_i E^i \quad (1.41)$$

where i is 1,2,3,4,..... can be tried. When this is substituted in eq. 1.40, and terms of the same order are collected, this results in

$$\frac{d^2r_1}{dt^2} + 2\gamma\frac{dr_1}{dt} + \omega_0^2r_1 = -\frac{e}{m}E, \quad (1.42)$$

$$\frac{d^2r_2}{dt^2} + 2\gamma\frac{dr_2}{dt} + \omega_0^2r_2 = \mu r_1^2. \quad (1.43)$$

From eq. 1.43 it follows that the displacement of the electrons in the material is no longer proportional to the applied field. The nonlinearity is $r_2 = a_2 E^2$, which corresponds to the first nonlinear term in the polarization (see eq. 1.31). When higher-order terms of r are also taken into account, it is found that they contribute to higher-order nonlinearities.

1.3 Crystals

In a non-centric crystal, *i.e.* crystals without a symmetry centre, the nonlinear susceptibility $\chi^{(2)} \neq 0$. In crystals with a symmetry centre and in isotropic matter as well $\chi^{(2)}$ must be zero by definition. This can be argued as follows. From eq. 1.31 it is clear that:

$$-\vec{P} = -\chi^{(1)}\vec{E} - \chi^{(2)}\vec{E}\vec{E} - \chi^{(3)}\vec{E}\vec{E}\vec{E} - \chi^{(4)}\vec{E}\vec{E}\vec{E}\vec{E} \text{ etc.} \quad (1.44)$$

Using the symmetry operator I_{op} gives:

$$I_{op}\vec{P} = -\vec{P}, \quad (1.45)$$

$$I_{op}\vec{E} = -\vec{E} \quad (1.46)$$

Applying the symmetry operation on eq. 1.31 gives:

$$I_{op}\vec{P} = -\vec{P} = -\chi^{(1)}\vec{E} + \chi^{(2)}\vec{E}\vec{E} - \chi^{(3)}\vec{E}\vec{E}\vec{E} + \chi^{(4)}\vec{E}\vec{E}\vec{E}\vec{E} - \text{etc.} \quad (1.47)$$

Comparing eq.1.44 with eq.1.47 shows that consistency only exists for $\chi^{(2)}\vec{E}\vec{E} = -\chi^{(2)}\vec{E}\vec{E}$, hence, $\chi^{(2)}$ must be zero. The same holds for all even powers of the susceptibility expansion. Thus, in all media with inversion symmetry have $\chi^{(2n)} = 0$.

The nonlinear susceptibility is defined to be $\chi^{(2)} = 2d_{ijk}$. The susceptibility χ_{ijk} and nonlinear efficiency d_{ijk} are tensors; the index i can have the values 1,2 or 3 corresponding to the respective crystal axes x , y or z and jk can have the values $jk = 1, 2, 3, 4, 5$ or 6 corresponding to the combinations of axes xx , $xy = yx$, $xz = zx$, yy , $yz = zy$ and zz . For instance, for the term d_{31} the polarization of the pump wave is along the z -axis, the polarizations of the generated waves are along the x -axis.

1.3.1 Phase matching

The phase matching conditions are depicted in fig. 1.2 and given by eqs. 1.2 or 1.5. Phase matching means that the wave generating the polarization and the generated waves (the three interacting waves) are in phase over the interaction region, so the microscopic contributions of the generated polarization of each individual dipole in the crystal can interfere constructively, adding up to a macroscopic field. Only after this constructive interference the nonlinear effect can be observed.

The \vec{k} -vector is defined as:

$$\vec{k}_i = \frac{\omega_i n(\omega_i)}{c} = \frac{\omega_i}{v(\omega_i)} = \frac{2\pi n_i}{\lambda_i} = 2\pi n_i \sigma_i. \quad (1.48)$$

Here $v(\omega_i)$ is the phase velocity, $n(\omega_i)$ the refractive index and λ_i the wavelength. σ_i is the wavenumber. To achieve phase-matching, the phase velocity of the generated waves (while travelling through the crystal) should equal the phase velocity of the pump wave in a parametric process. This can be achieved in a birefringent crystal which has different indices of refraction along the different crystal axes. In birefringent crystals, waves with different wavelength can travel at the same speed (so in phase) when their polarization directions are along different crystal axes. To fulfil phase matching, the generated waves and the applied wave must have different polarizations to control their propagation velocities. Recently, periodically-poled crystals have become available. In these crystals phase matching is pre-

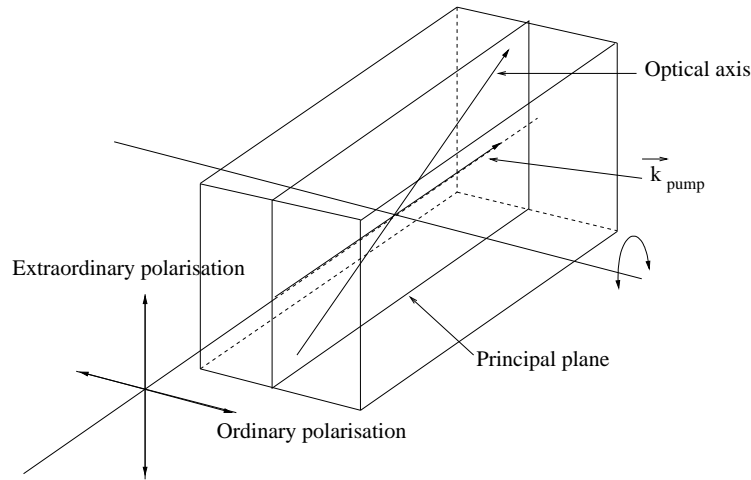


Figure 1.7: *An uniaxial birefringent crystal. The principal plane of the crystal is the plane of the wave vector \vec{k} and the optical axis of the crystal. An ordinary polarized wave has a polarization perpendicular to this plane and an extraordinary polarized wave has polarization in the principal plane.*

served by periodic poling of the nonlinear crystal. At the point where the generated wave(s) and the applied wave are out of phase by 90° the direction of the crystal axes is reversed, so that the phase differences are reduced again. This poling period of nonlinear crystals available is typically of the order of a few (tens of-) micrometers.

In the case of periodic poling, the choice of the d_{xyz} to be used in a nonlinear conversion process is free. This may lead to enhanced conversion efficiencies. In case of birefringent phase matching, *e.g.*, d_{33} in LiNbO_3 can never be used because the generated wave has the same polarization as the applied wave and hence they will run out of phase quickly and the generated wave will not build up power.

The quality of the periodically poled crystals that are available on the current market is unfortunately still not sufficiently good. When using visible radiation absorptions, gray tracking and light-induced index-of-refraction effects play a role. All experiments described in this thesis are therefore based on birefringent phase-matching.

For the definitions of the polarization directions of the light and the plane in the crystal see fig. 1.7. The principal plane of the crystal is the plane in which both wave-vector \vec{k} of the incoming light beam and the optical axis of the crystal lie. An ordinary polarized light wave has a polarization perpendicular to this plane and is called ordinary because the index of refraction n_o is constant. The extraordinary polarized light wave has its polarization in the principal plane and has an index of refraction n_e that depends on the angle with respect to the optical axis. A uniaxial crystal is called positively birefringent when $n_e > n_o$ and negatively birefringent for $n_e < n_o$, see fig. 1.8.

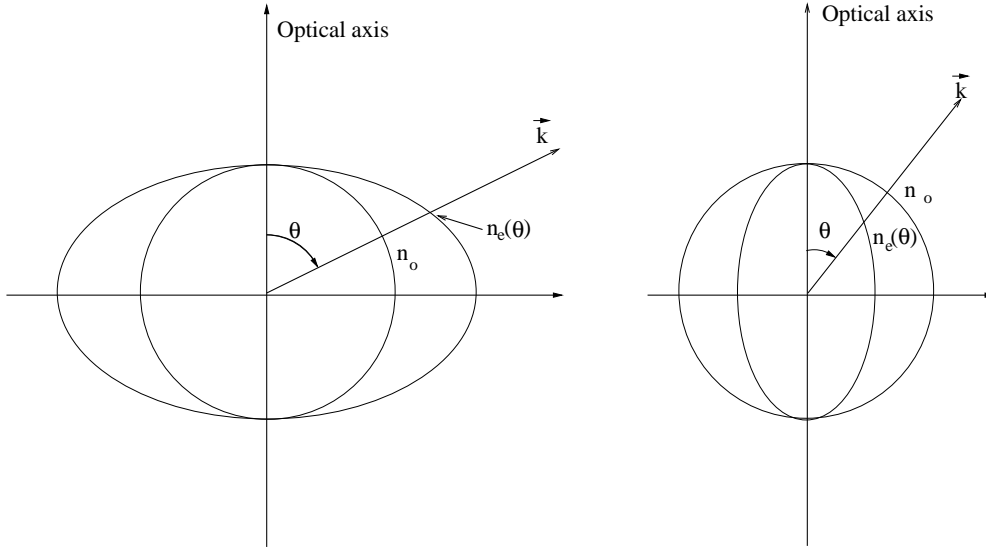


Figure 1.8: *Dependence of the angle Θ between the wave vector k and the optical axis of a positive (right) and negative (left) birefringent crystal.*

Two major types of birefringent phase matching are known for optical parametric devices,

$$\text{type - I} : e_{\text{pump}} \rightarrow o_{\text{signal}} + o_{\text{idler}}, \quad (1.49)$$

$$\text{type - II} : e_{\text{pump}} \rightarrow o_{\text{signal}} + e_{\text{idler}}. \quad (1.50)$$

Or, in the case of sum-frequency mixing:

$$\text{type - I} : o_{\lambda_1} + o_{\lambda_2} \rightarrow e_{\lambda_3}, \quad (1.51)$$

$$\text{type - II} : o_{\lambda_1} + e_{\lambda_2} \rightarrow e_{\lambda_3}. \quad (1.52)$$

The most commonly used nonlinear crystals for frequency mixing and optical parametric oscillators are β -barium borate (β -BaB₂O₃, BBO), lithium triborate (LiB₃O₅, LBO), potassium titanyl phosphate (KTiOPO₄, KTP) and lithium niobate (LiNbO₃). Some of these materials were developed not so long ago; BBO in 1985 and LBO in 1989, both by the group of Chen [5, 6]. For the work described in this thesis BBO was used for the pulsed OPOs, LBO and BBO were used in the cw frequency mixing experiments.

1.3.2 Walk-off

For any phase matching other than in the crystal's xy plane, the interacting waves will physically separate from each other, since they have orthogonal polarizations. This separa-

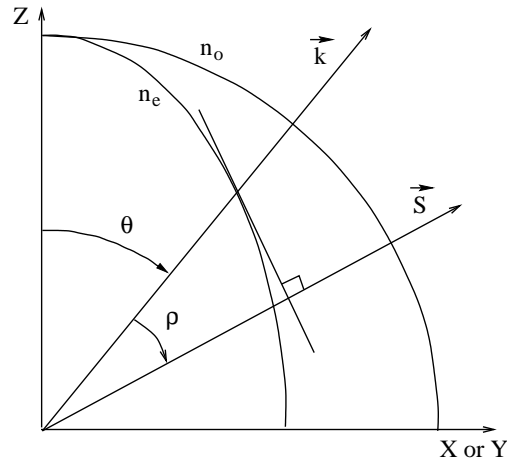


Figure 1.9: The walk-off angle ρ between the wave vector \vec{k} and the Poynting vector \vec{S} in a negative birefringent crystal.

tion is called "walk-off". The propagation direction of the energy of a wave in a crystal is given by the Poynting vector (\vec{S}). The direction of the Poynting vector is the normal to the tangent of the wave vector (\vec{k}) and the curve of the refractive index (see fig. 1.9). For the ordinary wave the curve of the index of refraction $n_o(\theta)$ is a circle, and the direction of the Poynting vector (\vec{S}) is equal to the direction of the wave vector (\vec{k}). For the extraordinary wave, on the other hand, the curve of the index of refraction $n_e(\theta)$ is an ellipsoide. Here the wave vector and the Poynting vector do not overlap. The walk-off angle ρ is defined as the angle between the wave vector of the generated wave(s) and the Poynting vector \vec{S} (the direction of the energy propagation). From fig. 1.9 it is seen that when $\theta = 0^\circ$ or $\theta = 90^\circ$, the walk-off angle ρ is zero. However, phase matching cannot take place along the optical axis of the crystal ($\theta = 0^\circ$), since then $n_o = n_e$. It is possible to phase match at $\theta = 90^\circ$, this is known as noncritical phase matching. Obviously, in this case the angle cannot be tuned, so phase matching is achieved by changing the temperature of the crystal, which changes the refractive index n_e .

When the walk-off is too large, the interacting waves will not overlap spatially in the entire crystal, and the conversion process will be terminated. When walk-off is present, but a longer nonlinear interaction length is desired, two separate crystals can be used instead of one longer crystal. The second crystal has to be oriented such that the optical axis is at an angle of 180° with respect to the optical axis of the first crystal. Hence, the walk-off in the first crystal is compensated in the second crystal.

1.4 Optical parametric oscillators

The first source of coherent optical radiation was the ruby laser, emitting light at 694.3 nm. This laser was created in 1960 by Maiman [8]. In 1961, Franken et al. [9], observed radiation at the doubled frequency of a pulsed ruby laser, when the light was passed through a quartz crystal. However, because of phase mismatch between the waves during the propagation in the crystal, the output of the generated second harmonic light was very low. One year later, Giordmaine [10] and Maker et al. [11] proposed independently, at the same time, a method to match the phase velocities of the fundamental and frequency doubled waves. They suggested to use the difference in the refractive indices for different polarizations in an optically anisotropic nonlinear crystal. The conversion efficiency was enhanced from 10^{-12} to several 10%. In this period also the first sum-frequency and difference-frequency mixing experiments were performed [12] and [13]. The first observation of optical parametric oscillation was made in 1965 by Giordmaine and Miller [14] in lithium niobate.

Pulsed optical parametric oscillators often exhibit a broad spectral bandwidth which is not desirable for many applications. Several mechanisms have been explored to reduce this bandwidth: injection seeding with a narrow-bandwidth (diode)laser [7], [15] and the use of frequency selective intra-cavity elements such as etalons [16]. Several successful attempts to reduce the bandwidth of OPOs have been reported using a grating at grazing incidence angle in the cavity [17], [21]. With this technique, single longitudinal mode (SLM) operation can be obtained. In this thesis (chapters 2 and 3) the use of a grating at grazing incidence angle has been further investigated.

1.4.1 Fourier-transform-limited pulses

One of the important performance criteria for pulsed optical parametric oscillators, in particular for spectroscopic applications, is their spectral bandwidth. The minimal bandwidth of a pulse of light is limited by its duration. This limit is determined by the product of spectral bandwidth and pulse duration and gives the relation between the minimal bandwidth $\Delta\omega_p$ and the pulse duration τ_p . The pulses generated by OPOs are usually of Gaussian shape. The temporal dependence of the field is:

$$E(t) = E_0 e^{-(t/\tau_G)^2} \quad (1.53)$$

The minimum duration x bandwidth product is:

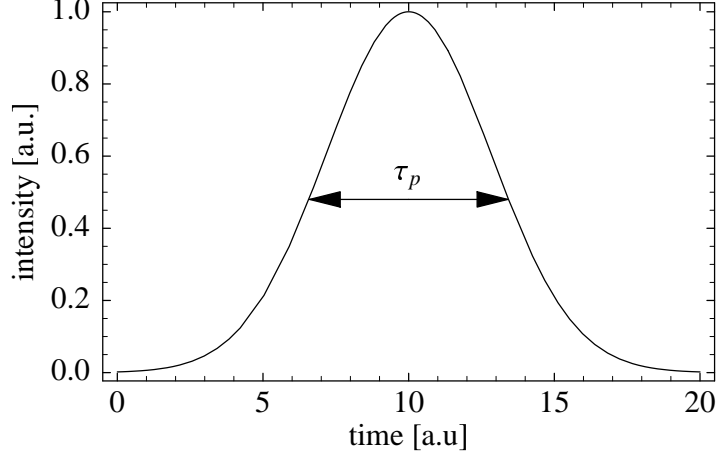


Figure 1.10: *Gaussian pulse, the full width at half maximum is τ_p .*

$$\Delta\tau_p\omega_p = 2\pi\Delta\nu_p\tau_p \geq 2\pi c_B \quad (1.54)$$

The constant c_B depends on the pulse shape. The pulse duration of a Gaussian pulse can be written as:

$$\tau_p = \sqrt{2\ln 2}\tau_G \quad (1.55)$$

The full-width-half-maximum (FWHM) of the spectral intensity distribution of a Gaussian is:

$$\Delta\omega_p = \frac{1}{\tau_G}/\sqrt{8\ln 2} = 2\pi\Delta\nu_p \quad (1.56)$$

So the minimal pulse-duration-bandwidth product in this case is:

$$\Delta\nu_p\tau_p = \frac{2\ln 2}{\pi} = 0.441 \quad (1.57)$$

1.4.2 Grazing incidence cavity

Among the various techniques for bandwidth narrowing (see review in ref. [22]) the use of an OPO cavity containing a grazing-incidence (GI) grating has been successful [17]. Even single longitudinal (SLM) mode operation can be obtained. In a Grazing Incidence OPO (GIOPO) device the favourable intrinsic properties of a nonlinear crystal can be exploited optimally as far as the tunability over a wide spectral range is concerned. SLM operation and a large scan range have been demonstrated with a GIOPO based on a beta-barium-borate (BBO) crystal, covering a signal range from 460 to 630 nm [18]. Chapter 2 and 3 of this thesis describe GIOPOs based on BBO crystals. In fig. 1.11 a schematic of a grazing

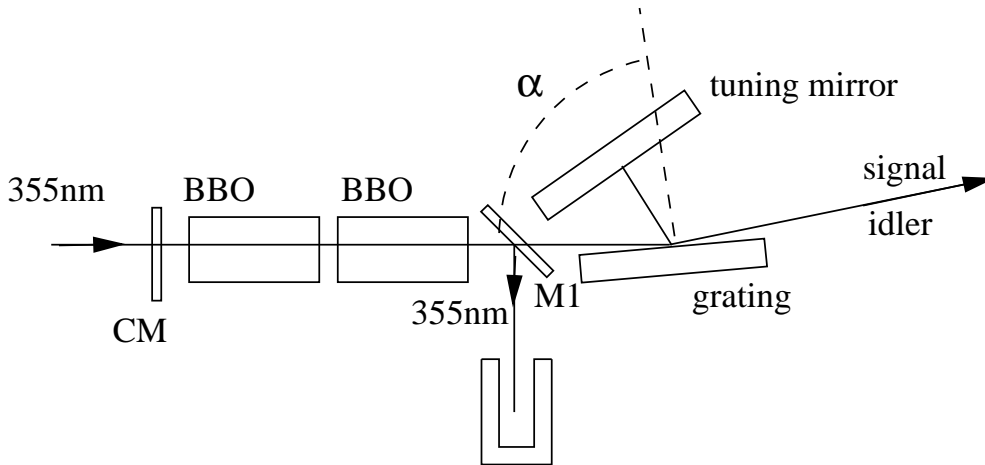


Figure 1.11: Schematic of a cavity with a grating at grazing incidence angle. *CM* is a cavity mirror (high transmission (HT) for pump wavelength), *M1* is a dichroic mirror high reflector for the pump wavelength and HT for signal and idler waves. The GI-angle α is measured between the incoming light beam and the plane perpendicular to the surface of the grating.

incidence cavity is shown.

In comparison with the alternative technique of bandwidth narrowing by injection seeding of a pulsed OPO [23], [19], the GI grating configuration appears to be potentially more cost-effective as it does not require a series of cw single-mode seed sources to cover a wide tuning range. Unfortunately, gratings at a grazing incidence angle exhibit a low reflection efficiency, giving rise to a higher threshold of the OPO system. Care should be taken that the damage threshold of the nonlinear crystals is not exceeded. To compensate for extra cavity losses and hence the higher oscillation threshold, a second nonlinear crystal is implemented in the cavity, in a walk-off compensated configuration.

Also, when a grating is used in the OPO cavity the cavity length increases, implying that the longitudinal mode-spacing decreases. This results in a lower selectivity when single longitudinal mode operation is desired. To obtain a strong suppression of the neighbouring modes, the grating has to be positioned at an angle of about 89 to 89.5 degrees, with as a consequence a high oscillation threshold and low output power. To overcome the problems of the narrow-bandwidth oscillator, the output can be further amplified in a seeded power oscillator. This configuration is described in chapter 2 of this thesis.

To minimise cavity round-trip losses, the grating should be chosen such that the reflection efficiency is as large as possible. Care should be taken that no generated light is diffracted in higher diffraction orders which can not resonate in the cavity. This implies that only a first order diffraction is desired. The number of lines per mm of the grating should be chosen

such that only this first order diffraction can occur for the desired wavelength. In the grazing incidence configuration the zeroth order diffraction of the grating is used to couple light out of the cavity. To optimise the gratings performance, also the material of the grating should be considered; for systems oscillating in the visible wavelength range the gratings are made of aluminium. For GIOPOs oscillating on the idler wavelength (*e.g.*, 1530 nm and 1930 nm) the gratings are made of gold for higher reflectance.

Further improvements of GIOPOs, such as new cavity designs and pump geometries, however, are desirable. In chapter 3, an alternative grazing incidence cavity is presented, using two prisms and only one nonlinear crystal. Recently, periodically-poled nonlinear crystals have been successfully used as well for SLM-GIOPOs in the laboratory [20].

1.4.3 Relay imaging

For optical parametric oscillators, nonlinear optical devices or optically pumped lasers such as Ti:S or dye lasers, the beam quality of the pump laser is of great influence on the characteristics of the generated light and the efficiency of the pumping process. For the pulsed OPOs as described in the chapters 2 and 3 of this thesis, a technique called 'relay imaging' is used to make optimal use of the beam quality of the pump laser. In relay imaging the cross-section of a laser beam is imaged over a (large) distance using a two-lens system (with focal lengths f_1 and f_2 respectively). This cross-section is imaged at a distance $2f_1+2f_2$ [24]. This technique assures a clean image of the pump beam with an appropriate energy density, a flat phase front and no divergence. This leads to better operation of the OPO and also protects optics from damaging. Normally, after travelling for more than one meter through air, the beam profile of a laser already gets distorted. Moreover, interferences of the transversal modes of the laser can lead to hot-spots, which can have high energy densities. Using this technique we have achieved nice beam profiles at distances up to 5 meters behind the laser-head.

It should be noted that in the object plane used for relay-imaging an optimal beam profile must be available, *e.g.*, the cavity waist of a Gaussian beam. For the OPO experiments described in this thesis a the third harmonic of a pulsed Coherent Infinity Nd:YAG laser has been used. This laser makes use of the relay-image technique for the amplification of the pulses. The beam profile of a cw seed ring-laser is relay-imaged onto a set of Nd:YAG rods, where the pulsed amplification takes place. The plane of the Nd:YAG rods is in its turn imaged onto the position of the second- and third- harmonic crystals. Since the beam profile is of good quality here, the second and third harmonic conversion efficiencies are

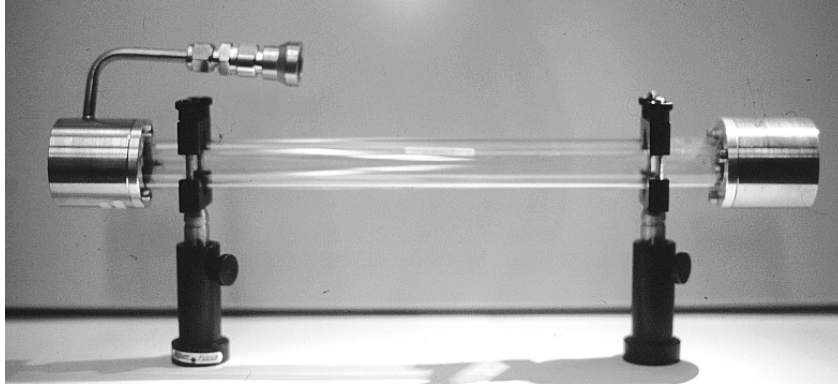


Figure 1.12: relay imaging system. The focal plane is situated in the glass vacuum tube to avoid air-breakdown. The glass tube is closed by the two aluminium lens mounts, which are held by rubber o-rings. On the left side the tube with the connection/valve to evacuate the system.

high. The plane containing these crystals is the object plane that is relay imaged into the parametric oscillators.

When an object placed in the focal plane in front of a converging lens is illuminated with a parallel beam of light, a Fourier-transform of the object will be made in the back-focal plane (Σ_t) of the lens [25]. This is called the power spectrum. When a second lens is placed at a distance f_2 behind the image plane of the first lens, again an image is made of this plane Σ_t , and a Fourier-transformation (or an inverse transformation) will be made, which means the original object is obtained again, see figure 1.13. The power spectrum consists of spots of the diffraction pattern. Each spot position corresponds to a specific spatial frequency in the object plane. The spatial frequencies are proportional to the distance of the spot from the optical axis. Higher spatial frequencies are imaged further away from the optical axis.

A lens with an infinite aperture can transmit all spatial frequencies. As lenses do not have an infinite aperture, they will act as a low-pass filter. Most frequencies will be transmitted, but spatial frequencies above a certain value will be rejected. This characteristic of a lens-system is used to "clean" the beam profile, *e.g.*, wavefront distortions due to scatter on dust particles are filtered out, because they correspond to higher spatial frequencies.

In the focal plane between the two lenses the intensity of the light can be very high. When using pulsed lasers in this focus air-breakdown may occur, which obviously leads to quality loss of the beam. To avoid breakdown, the lenses can be mounted inside a vacuum chamber. In figure 1.12 the system used for the experiments described in the chapters 2

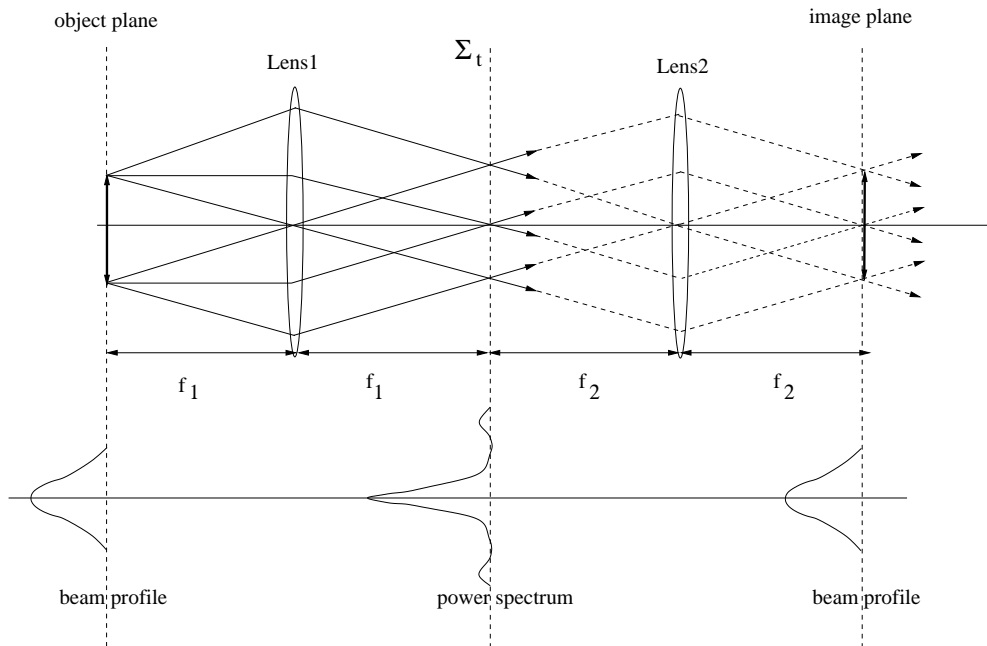


Figure 1.13: *relay imaging system.*

and 3 is depicted. The focussing lenses act also as windows for the vacuum chamber. This reduces the number of optical elements (and hence the amount of power loss) in the laser beam. Using a turbo pump, the pressure in the vacuum system is reduced to 10^{-3} mbar.

To demonstrate the effect of relay imaging, a beam profile cross-section image is taken, using a Pulnix CCD camera. In fig. 1.14 these cross-sections of the beam, recorded at different positions in the beam path, are shown. The second harmonic crystal inside the Nd:YAG laser is the object plane for the relay image. This crystal has a small imperfection, a small air bubble. In the imaged relay plane, this small air bubble is clearly visible, indicating a proper image of the object plane is made.

1.4.4 Spectrum analyser

To control the SLM operation of pulsed OPOs an optical spectrum analyser has been built. This spectrum analyser consists of a Fabry-Perot (FP) interferometer and a CCD camera. A small fraction (1%) of the light generated in the OPO is coupled into single-mode fibers and used for analysis. This light is split into two parts, one part is sent to the spectrum analyser, the other part is sent to the Lambda-meter to determine the absolute wavelength.

The wavelength meter (type ATOS Lambda-meter LM-007) consists of a temperature-

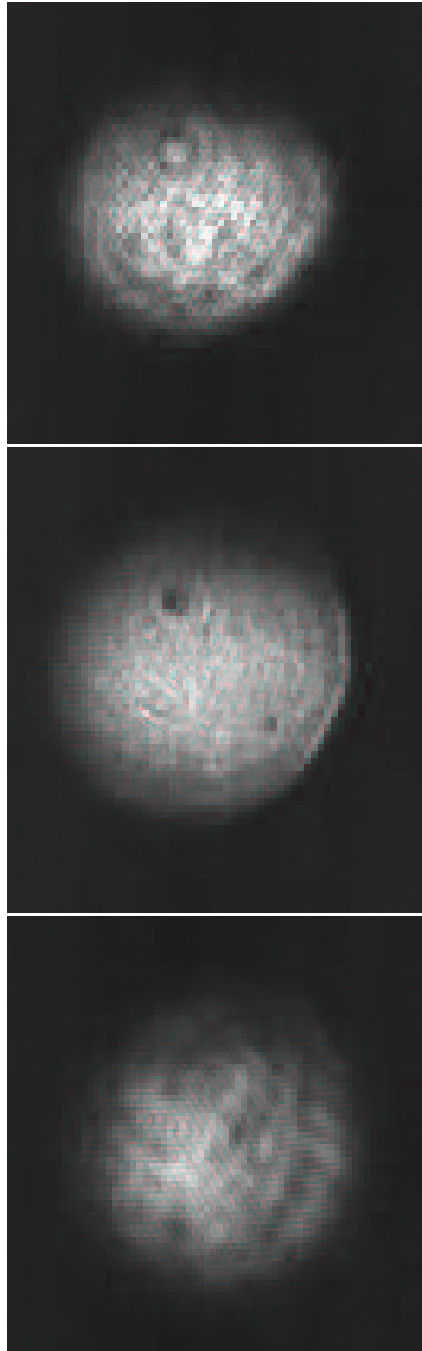


Figure 1.14: *Beam cross-sections taken with a CCD camera, at different positions in the beam path. The centre image is taken at the position of the relay plane, the second harmonic crystal with the air bubble is imaged very clearly at this position. Note also the homogeneous intensity distribution. The higher and lower images are taken resp. 6 cm before and 20 cm behind the relay plane.*

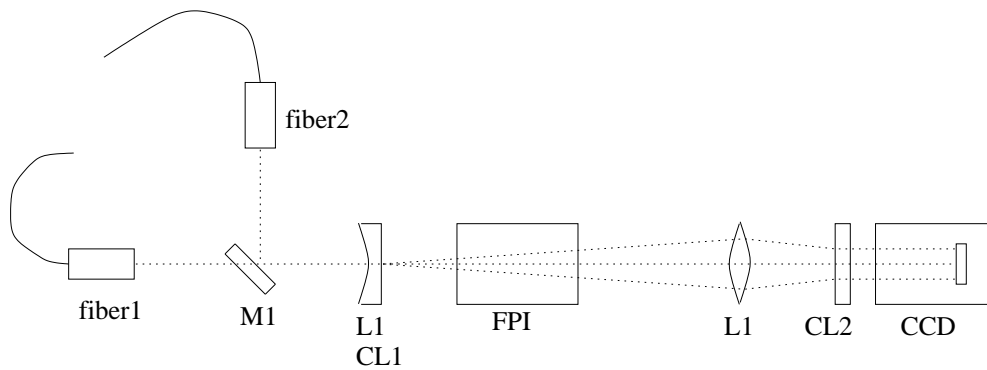


Figure 1.15: *Spectrum analyser system. CL1 and CL2 are cylindric lenses. L1 is a spherical lens, FPI is a 9 Ghz air spaced Fabry Perot interferometer, CCD is a Pulnix CCD camera. Light is coupled in via the two fibers. Two OPOs (or seed OPO and power oscillator) can be analysed at the same time.*

stabilised monolithic quartz block containing four neon filled Fizeau interferometers with different free spectral ranges (FSR) (resp. 1000, 50, 2.7 and 0.127 cm^{-1}). This system can measure wavelengths between 400 and 1100 nm with an accuracy of 10^{-5} nm ($\approx 5\text{ MHz}$ at 800 nm). The interferometer with a FSR of 0.127 cm^{-1} (3.8 GHz) and a finesse of 10 could in principle be used as a spectrum analyser as well. However, the cavity length of the seed OPO (GIOPO) corresponds to a FSR of 1.9 GHz. When the OPO starts to run in two longitudinal modes, an additional peak will appear in the FP spectrum exactly in the middle between two peaks of the different etalon orders. Hence, it will not be possible to determine to which etalon order the new peak belongs, and in which way the cavity length has to be adjusted. Therefore, this interferometer cannot be used to detect multi-mode operation of the OPO.

For this reason an additional FP-spectrum analyser has been built to control the single-mode operation of the OPO. A schematic of the setup is shown in fig. 1.15. This spectrum analyser consists of a CCD camera (Pulnix TM6AS) mounted behind an air-spaced Fabry-Perot interferometer (Melles Griot). The air-spaced interometer is coated for wavelengths between 400 nm and 600 nm, has a FSR of 9 GHz and a finesse of 20. Light is coupled in via a single-mode fiber. At the exit of the fiber the light is coupled out via a microscope objective (20x). A negative cylindrical lens ($f = -10\text{ cm}$) is used to make a slightly divergent beam. Next the light passes through the FP interferometer and is imaged by a second cylindrical lens onto the chip of the CCD camera (on which no imaging lens is mounted). To prevent that stray light reaches the CCD chip, the entire spectrum analyser is built into a black box.

In Fig. 1.17 a typical frame-grabber picture of the mode structure of the narrow band-

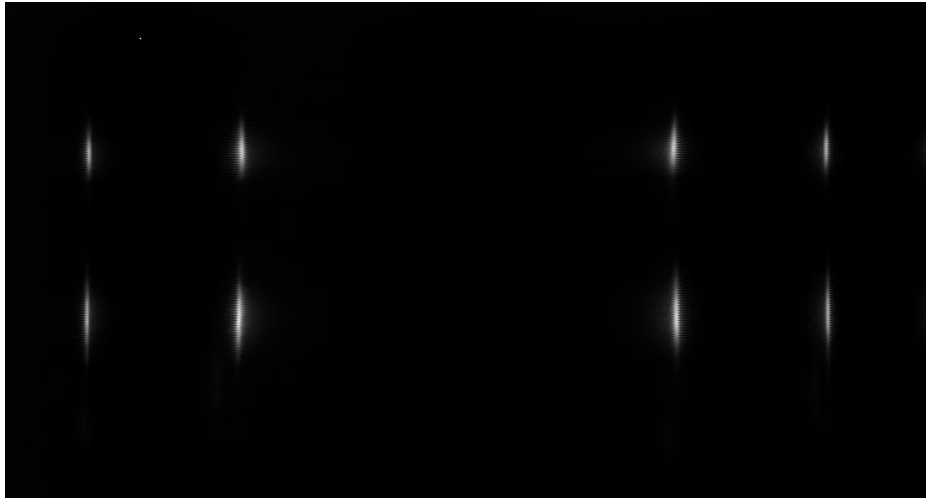


Figure 1.16: *CCD-camera image, obtained using the FP etalon of a seed OPO (upper part of graph) and a power amplifier (lower part of the graph). A cross-section is taken to obtain the intensity plot fig.1.17*

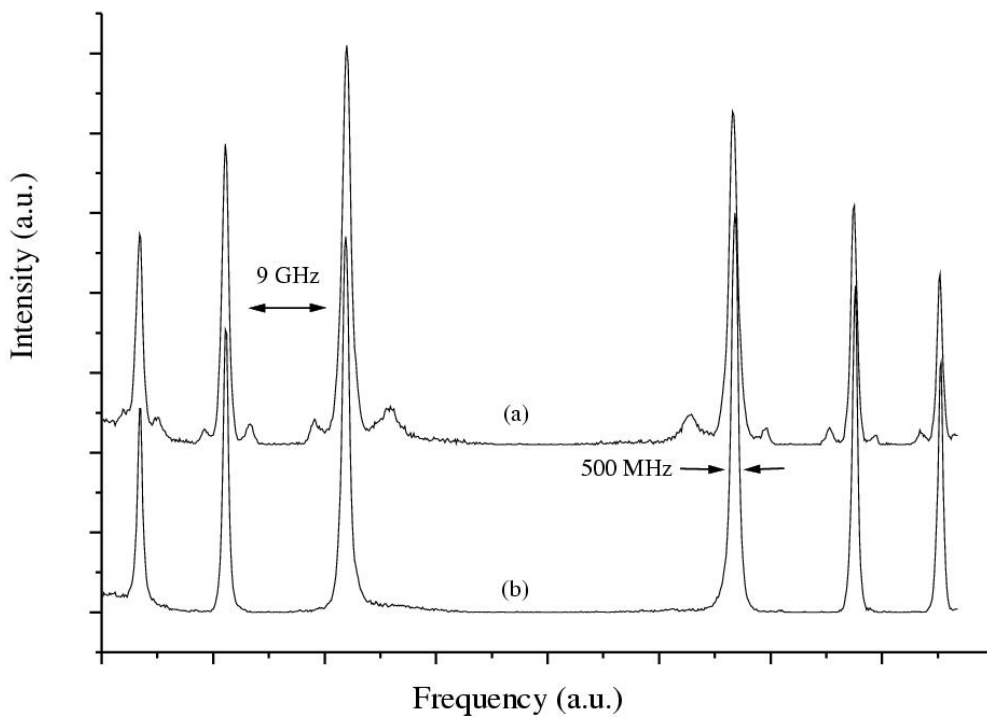


Figure 1.17: *Spectrum recorded using the FPI-spectrum analyser of a seed OPO (a) and a power oscillator (b).*

width seed OPO (a) and the power oscillator (b) are given. Single-mode operation of the OPO is controlled by this spectrum analyser using of a feedback program written in a combination of C++ and Labview languages. When side modes occur in the FP spectrum of the OPO, software calculates the desired shift in the positions of the spectrum analyser

fringes of the OPO. This desired shift is converted to a voltage to adapt the OPO cavity length by a piezo-transducer. The wavelength and Fabry-Perot spectra could be measured only in the visible region due to the coupling fiber used and the etalon coating. To determine the infrared idler wavelengths generated in the OPOs, the software calculates the wavelength of the infrared idler wave from a measurement of the signal wavelength and the wavelength of the second harmonic of the pump laser. From this the wavelength of the third harmonic –the pump wavelength– follows, as well as the idler wavelength.

1.5 Continuous wave frequency mixing

One of the complications of frequency mixing and optical parametric generation is that powerful radiation fields are needed to generate observable nonlinear effects. Hence generating continuous wave (cw) wavelengths using these techniques is difficult. Pulsed lasers, on the other hand, are suitable for both applications because of high peak intensities. In the last decades new nonlinear materials such as BBO, LBO and KTP have been developed with large nonlinear conversion efficiencies. Moreover, the technique of periodic poling of nonlinear crystals has been developed, which enables phase matching for almost any wavelength and polarization combination. This allows for the use the highest effective nonlinearity of crystals which was previously not feasible using conventional birefringent phasematching. For the cw-frequency mixing experiments described in chapter 4 of this thesis an enhancement cavity is used. In these cavities the intensity of the radiation fields can be enhanced, leading to more effective frequency mixing processes.

1.6 Enhancement cavities

An external enhancement cavity (EEC) is a frequently used tool for continuous wave frequency doubling, *e.g.*, of tunable dye or Ti:Sapphire lasers [29]. These cavities can also be used for frequency mixing purposes (in fact, second harmonic generation is a special case of frequency mixing, where the two input photons have the same wavelength). An EEC is used to increase the intensity of the EM field by locking it resonantly to the laser wavelength. The power P_{out} generated by a frequency-mixing process has the dependence [26]:

$$P_{\text{out}} = \gamma P_{\text{in1}} P_{\text{in2}}, \quad (1.58)$$

in which $P_{\text{in}1}$ and $P_{\text{in}2}$ are the power of the two incident laser fields respectively, and γ is the nonlinear coefficient of the process, which contains frequencies of the interacting waves, the crystal length and the optical beam geometry. Resonantly enhancing both wavelengths in the cavity leads to:

$$P_{\text{out}} = \gamma(A_1 P_{\text{in}1})(A_2 P_{\text{in}2}), \quad (1.59)$$

where A_1 and A_2 are the cavity enhancement factors for the two interacting waves: λ_1 and λ_2 respectively, and $P_{\text{in}1}$ and $P_{\text{in}2}$ are the respective powers of the light coupled into the enhancement cavity. The enhancement factor A depends on the quality of the resonator:

$$A = \frac{1 - R}{(1 - \sqrt{RV})^2}, \quad (1.60)$$

Here, R is the reflectivity of the input coupler, and $(1 - V)$ is the cavity loss per round-trip. V can be calculated using

$$V = \frac{e^{2\pi/F}}{R}, \quad (1.61)$$

with F the finesse of the cavity with the crystal inside. The enhancement is optimal when cavity losses (*e.g.*, on the crystal surfaces and conversion losses) equal losses of the input-coupler, $R = V$. This is the so-called "impedance matching condition".

The cavity used for the experiments on frequency doubling and tripling of a Ti:S laser, as described in chapter 4 of this thesis, is depicted in fig. 1.18. The cavity has a travelling wave configuration, which has several advantages. In a standing wave configuration the light rejected by the input coupler reflects back into the laser, which may disturb the operation of that laser. In a running wave configuration (ring cavity) the input coupler is tilted with respect to the incoming beam, so this problem does not occur. Also, in a standing wave configuration the generated second harmonic light propagates both in forward and backward directions and combining these two beams is not easy. In a ring cavity, on the other hand, the second harmonic is generated in the forward direction only. Additionally, the tilted curved mirrors can be used to compensate for the astigmatism induced in a Brewster cut crystal. The conversion efficiency of the two different cavity types is similar.

For efficient operation of the enhancement cavity, it is very important that as much light as possible is coupled into the cavity. The in-coupling depends on several factors: the impedance matching, mode-matching and resonance condition (the locking system) are the most important.

The length of the cavity used is 0.80 meters, which implies a free spectral range of 375 MHz. The losses on the crystal surface are usually about 1% so the input coupler is chosen

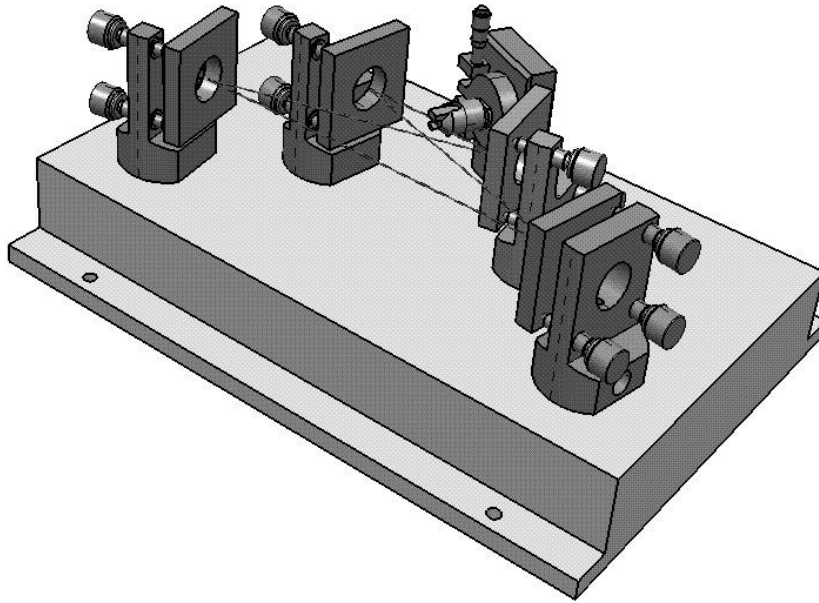


Figure 1.18: *An external enhancement cavity. The cavity is build up using "Lees" optical mounts, on a solid aluminium baseplate.*

to be 99%. The other mirrors are high quality high reflectors, so the typical finesse is about 300. In combination with the FSR of 375 MHz, this leads to a FWHM of the cavity fringes of 1.2 MHz. This is slightly larger than the linewidth of the Ti:S ring-laser ($\leq 900\text{kHz}$). If the finesse of the cavity would be too high the incoupling efficiency of the Ti:S light would decrease.

1.6.1 Mode matching

The laser beam that has to be coupled into the cavity must be shaped in such a way that the spatial overlap with the cavity modes is optimal. These cavity modes are determined by the curvature of the mirrors and the distance between respective mirrors. The cavity used has two curved and two flat mirrors. The bow-tie cavity has two cavity waists, one in-between the two curved mirrors, where the nonlinear crystal is positioned, the other one between the two flat mirrors. Using the ABCD-matrix formalism for an optical system [28], the cavity waists, the stability range and the confocal-parameters can be calculated. See fig. 1.20.

For paraxial rays at an initial position x_1 and with a slope α_1 , the ray- path can be

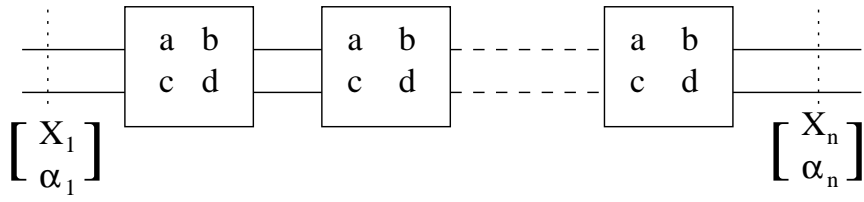


Figure 1.19: Periodic sequence of ABCD matrices to describe multiple reflections in an optical cavity.

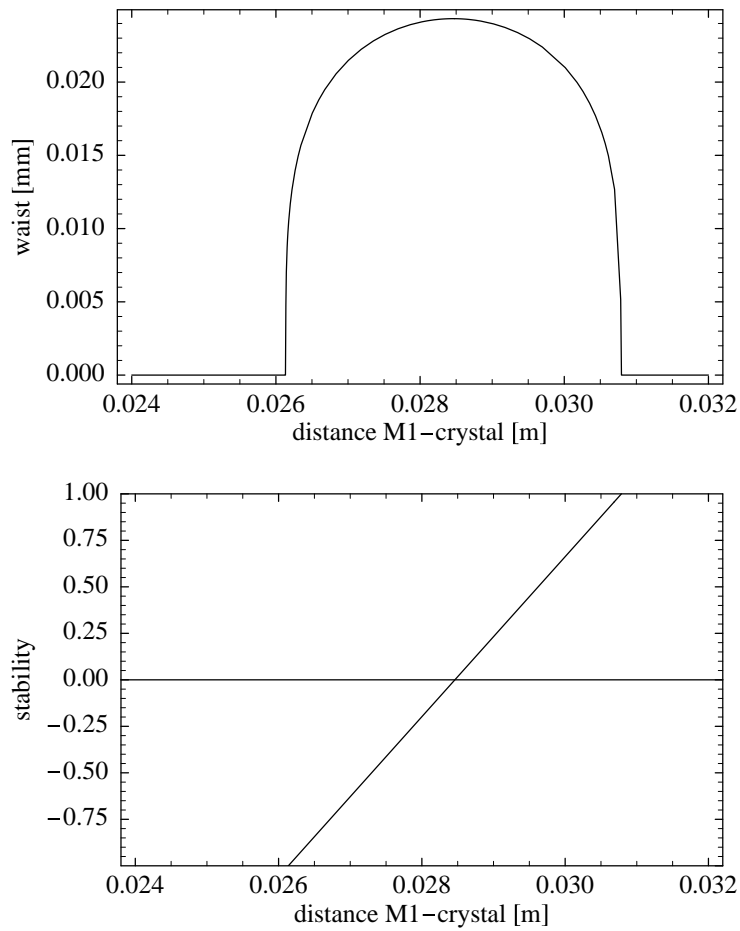


Figure 1.20: Waist size of the EEC and stability range ($-1 \leq s \leq 1$) of the EEC for concave mirrors with a radius of curvature of 75 mm and a total cavity length of 80 cm.

described by a ray transfer matrix:

$$\begin{pmatrix} x_2 \\ \alpha_2 \end{pmatrix} = \begin{pmatrix} a & b \\ c & d \end{pmatrix} \begin{pmatrix} x_1 \\ \alpha_1 \end{pmatrix}, \quad (1.62)$$

where x_2 and α_2 are the final position and slope respectively.

The propagation of light through the complete optical system (a sequence of lenses, nonlinear crystal and propagation distances through air) can be described by the product of series of matrices, resulting in a total system two-by-two ABCD matrix. Light rays that bounce back and forth inside a cavity can be described by a periodic sequence of this matrix (see fig. 1.19). Such a periodic sequence can be either stable or unstable. The determinant of the matrix must be unity, $AD - BC = 1$ (the stability requirement). The stability regime is where the trace obeys the inequality $|S| \leq 1$ where $S = \frac{1}{2}(A + D)$. In fig. 1.20 the stability regime and the cavity waist as a function of the mirror separation are given for the cavity parameters as used in the experiment. The cavity-waist between the curved mirrors is very tight; about $23\mu\text{m}$ and strongly focussed, the waist between the flat mirrors is larger (weakly focussed).

For practical reasons it is most simple to match the cavity waist between the two flat mirrors since it's not so tight and somewhat longer. Moreover, coupling light into the cavity through flat substrates is much more straightforward than through the curved mirrors. This waist has a diameter of $300\mu\text{m}$, for a cavity length of 80 cm and a resonating wavelength of 800 nm. Using a mode-match lens with a focal length of 40 cm, 86% of the light coming from the Ti:S laser could be coupled into the EEC.

1.6.2 Hänsch-Couillaud locking scheme

In 1980, Hänsch and Couillaud developed a locking scheme for a laser cavity [27] based on the polarization of the light reflected on the input coupler. This lock involves a simple setup, not using any modulation. The locking technique is based on a birefringent or polarization dependent cavity, for example containing a Brewster-cut crystal or a Brewster plate.

At the input-coupler, part of the linearly polarized light will be coupled in. This light can be decomposed into two orthogonal components: one parallel and the other perpendicular to the axis of the polarizer in the cavity. Only the parallel component sees a low loss cavity and experiences a cavity-length dependent (or frequency-dependent) phase shift.

Part of this light will leak out due to partial reflectivity of the input coupler. This light adds up to the perpendicular component, reflected by the input coupler, which serves as a reference. A relative phase change between these reflected components will make the resulting beam elliptically polarized.

If the cavity is exactly on resonance, the two polarizations will have a fixed relative phase difference and a linearly polarized wave will be reflected at the input coupler. The error signal for this situation has to be set on zero. If the cavity is off-resonance, the phase

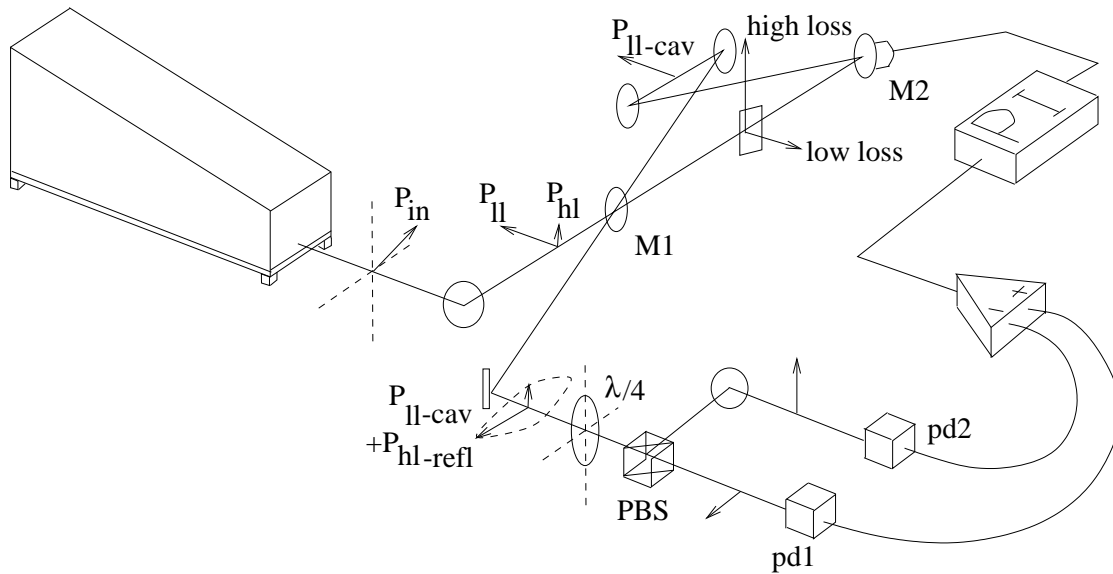


Figure 1.21: The laser polarization \vec{P}_{in} can be decomposed a parallel $\vec{P}_{||-cav}$ and a perpendicular component \vec{P}_{\perp} with respect to the polarizer axis. \vec{P}_{\perp} is reflected by the input-coupler M1 and is used as a reference. $\vec{P}_{||-cav}$ has a cavity-length dependent phase shift, when leaking out of the cavity at M1, it adds up to \vec{P}_{\perp} resulting in an elliptically polarized beam. This polarization is decomposed by a $\lambda/4$ plate and a polarising beam splitter (PBS). The intensities of both components are measured by two photodiodes (pd1 and pd2). In the logic element these two components are subtracted, and fed to the P-I servo.

difference is non-zero, and an elliptical polarization results. The handedness of the elliptical polarization depends on the sign of the detuning from resonance.

To analyse the polarization of the reflected wave, the beam is split into two orthogonal components using a $\lambda/4$ plate. The intensities of both components are measured by two photodiodes. The diode signals are subtracted, this results in the error-signal. From this an error signal results that can be fed back to the cavity-piezo using a proportional-integrating controller and a high voltage amplifier (see fig. 1.21). It should be noted that when a polarization is used that is exactly parallel to the optical axis of the cavity polarizer, no error signal results. However, in practical situations a small perpendicular component is always available.

Bibliography

- [1] V.G. Dimitriev, G.G. Gurzadyan and D.N. Nikogosyan in "*Handbook of Nonlinear optical Crystals*" Vol **64**, 345 3rd rev. edition. A.E. Siegman, ed. (Springer, New York, 1992).
- [2] F. Zernike and John E. Midwinter "*Applied Nonlinear Optics*"(John Wiley and Sons, New York, 1973).
- [3] Y.R. Shen "*The principles of Nonlinear Optics*" (John Wiley and Sons, New York, 1984).
- [4] A. Yariv "*Quantum electronics*" third edition (John Wiley and Sons, New York, 1989).
- [5] C. Chen, B. Wu, A. Jiang, G. You, Scientia Sinica, Ser. B **28**, 235 (1985).
- [6] C. Chen, Y. Wu, A. Jiang, A. Wu, G. You, R. Li, S. Lin, J. Opt. Soc. Am. B **6**, 616 (1989).
- [7] A. Borsutzky, Quantum Semiclass. Opt. **9**, 191 (1997).
- [8] T.H.Mainman Nature **187**, 493 (1960).
- [9] P.A. Franken, A.E. Hill, C.W. Peters, G. Weinreich Phys. Rev. Lett. **7**, 118 (1961).
- [10] J.A. Giordmaine Phys. Rev. Lett. **8**, 19 (1962).
- [11] P.D. Maker, R.W. Terhune, M. Nicenoff, C.M. Savage Phys. Rev. Lett. **8**, 21 (1962).
- [12] R.C.Miller, A. Savage Phys. Rev. **128**, 2175 (1962).
- [13] A.W. Smith, N. Braslau IBM J. Res. Dev. **6**, 361 (1962).
- [14] J.A. Giordmaine, R.C.Miller Phys. Rev. Lett. **14**, 973 (1965).
- [15] J.M. Boon-Engering, W.E. van der Veer, J.W. Gerritsen, E.A.J.M.Bente and W. Hogervorst, Opt. Lett. **20**, 330 (1995).
- [16] Feature Issue on Optical Parametric Devices, J. Opt. Soc. Am. B **12** volume II (1995).
- [17] W.R. Bosenberg, D.R. Guyer, Appl. Phys. Lett. **61**, 387 (1992).
- [18] J.M. Boon-Engering, W.E. van der Veer, E.A.J.M. Bente, W. Hogervorst, Opt. Comm. **136**, 261 (1997).
- [19] A.V. Smith, W.J. Alford, T.D. Raymond, J. Opt. Soc. Am. B **12** (1995) 2253.
- [20] P. Schlup, G.W. Baxter, I.T. McKinnie, Opt. Comm. **176**, 267 (2000).
- [21] L.A.W. Gloster, I.T. McKinnie, Z.X.Jiang and T.King, J.M. Boon-Engering, W.E. van der Veer and W. Hogervorst, J. Opt. Soc. Am. B. **12**, 2117 (1995).
- [22] A. Borsutzky, Quantum Semiclass. Opt. **9**, 191 (1997).
- [23] G. Ehret, A.Fix, V.Wei, G.Poberaj, T.Baumert, Appl. Phys. B **67**, 427 (1998).
- [24] F.L. Pedrotti and L.S. Pedrotti, "*Introduction to optics*", 2nd edition (Prentice Hall, New Jersey, 1993)
- [25] Hecht, "*Optics*", University Press, 522 (1980)
- [26] M. Brieger, H. Busener, A.Hese, F.v. Moers and A. Renn, Optics Comm., **38**, 423

(1981).

[27] T.W. Hänsch, B. Couillaud, Optics Comm., **35**, 441 (1980).

[28] H. Kogelnik, B.Li, Applied Optics, **10**, Oct(1966).

[29] C.S. Adams and A.I. Ferguson, Opt. Comm. 79 3,4(1990) .

Chapter 2

A SLM optical parametric oscillator for spectroscopic applications

2.1 Abstract

We have developed a tunable, narrow-bandwidth nanosecond OPO system and applied it to spectroscopic studies. The system consists of a narrow-bandwidth grazing-incidence oscillator and a seeded power oscillator. Fourier-transform-limited 1.5 ns pulses are generated (bandwidth < 500 MHz) in the wavelength range of 435 nm up to 2000 nm with an energy up to 3.5 mJ at a pump energy of 22 mJ. Continuous scanning over 30 to 100 GHz (depending on wavelength) is demonstrated by recording the resonance line of the Hg atom at 253.7 nm and a vibrational transition of the CO₂ molecule at 1528 nm.

2.2 Introduction

An Optical Parametric Oscillator (OPO) is an attractive, highly efficient solid-state source of coherent radiation tunable over a wide wavelength range [1]. Free running OPO's, however, exhibit a broad spectral bandwidth which is not desirable for many applications. Several mechanisms have been explored to reduce this bandwidth: injection seeding with a narrow-bandwidth (diode)laser [2] and [3] and the use of frequency selective intracavity elements such as etalons [4]. Several successful attempts to reduce the bandwidth of an OPO have been reported using a grating at grazing-incidence angle in the cavity [5],[6]. However, cavity losses are high in such a configuration and, hence, the efficiency of these systems is low. Also they exhibit strong output power fluctuations. We have developed a new configuration which is basically a Master Oscillator Power Amplifier (MOPA) system. The narrow bandwidth master oscillator is a Grazing Incidence OPO (GIOPO). Its output seeds the Power OPO (POPO)(see fig. 2.1). This system provides a stable output power in a Single Longitudinal Mode (SLM) with an overall efficiency of 14.5%.

2.3 Experimental setup

The OPO system is pumped with the third harmonic of a Coherent Infinity Nd:YAG laser. This laser delivers SLM pulses of 3 ns duration at 355nm at a repetition rate of 1 to 100 Hz, with a top-hat intensity distribution in the relay plane of the laser. This top-hat intensity distribution makes it an excellent pump laser for optical parametric oscillators. To maintain the intensity distribution of the laser beam, it is relay-imaged into both OPO cavities using two telescopes. These telescopes are also used to reduce the beam diameter of the pump laser. The telescope for the GIOPO has a magnification ratio of 2.75:1, for the POPO a ratio of 2.2:1. Both GIOPO and POPO are pumped with 11mJ from the Nd:YAG laser at 355nm.

The GIOPO consists of two uncoated 28° type-I BBO crystals (10 mm × 5 mm × 5 mm) in a walk-off compensated configuration. The pump light is coupled into the cavity via a flat end-mirror, that is highly reflective for the signal wave. Behind the crystals, the pump light is coupled out through a dichroic mirror to prevent grating damage by the pump light. The grating is chosen such that only a first order reflection can occur. The first order reflection is retro-reflected into the cavity by the tuning mirror. The zero-order reflection of the grating provides the light coupled out of the cavity [7]. To improve the efficiency of the GIOPO, which is operated close to threshold, the residual pump light is coupled back into the cavity by a high reflecting mirror and used again in the amplification of the parametric waves. To prevent damage inside the pump laser by the retro-reflected light, an additional dichroic high reflector and beamdump for 355 nm light are placed between the second and third harmonic crystals.

Three sets of optics and gratings are used to cover the wavelength range from 435 nm to 2000 nm. A 2400 lines/mm grating and a set of high reflectors is used to oscillate signal waves from 465 nm to 600 nm with corresponding idler waves in the range of 1500 nm to 1000nm, a 1800 lines/mm device with a second set of high reflectors covers the signal wavelength range between 600 nm and 710 nm, with corresponding idler waves ranging from 1000 nm to 710 nm. The remaining wavelengths, signal waves between 430 nm and 465 nm and idler waves between 1500 nm and 2000 nm, are generated by resonating the idler wave in the cavity. The reflection efficiency of an infrared reflecting 750 lines/mm grating at grazing incidence angle is much higher than the reflection efficiency of blue light on a 3600 lines/mm grating in the same configuration.

Since a grating at a grazing-incidence angle has a low reflection efficiency (< 3%) [8], the GIOPO must operate close to threshold, to avoid damage of the BBO crystals by high

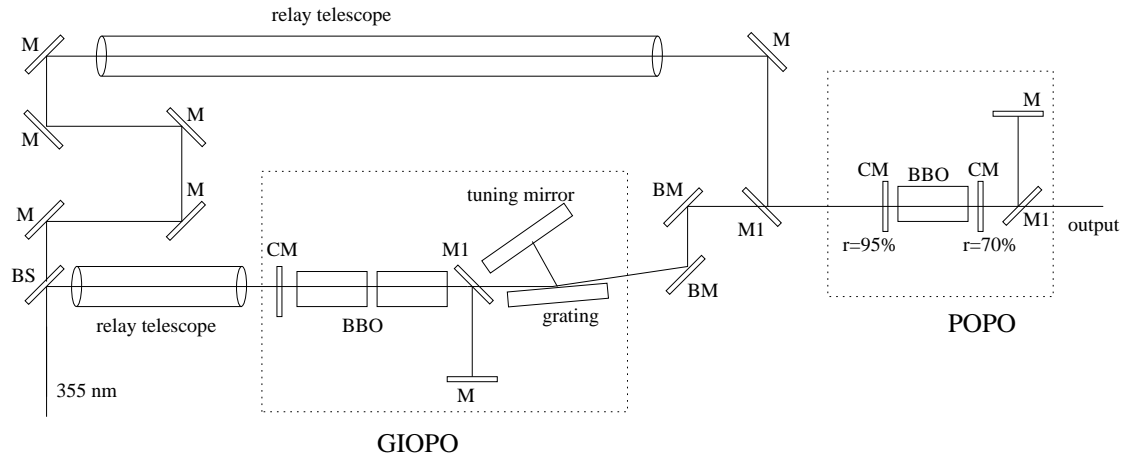


Figure 2.1: *Experimental setup. M: high reflecting mirror for 355 nm, M1: high reflecting mirror for 355 and high transmission for signal and idler waves, CM; cavity mirror, high reflector for signal or idler wave and high transmission for 355 nm, BM: bending mirror; high reflector for signal or idler wave, BS: 50% beam splitter for 355 nm.*

pump intensity. This results in low power output and strong intensity fluctuations. The oscillation threshold of the GIOPO is 8 mJ. It delivers 100 μJ pulses of 1.5 ns at 11mJ pump power. These pulses are further amplified in the POPO. For single mode operation, the cavity length can be changed by applying a voltage to the piezo on which the end mirror is mounted. Scanning can be achieved by changing the angle of the tuning mirror with respect to the grating. For this purpose the tuning mirror is also mounted on a piezo crystal. The scan range is limited to 100 GHz by the maximum expansion of the tuning mirror piezo. For scans of moderate length (<100 GHz) the phase matching angle of the crystals does not have to be adjusted.

The POPO consists of a BBO crystal (cut at 28° for type-I phasematching), 12mm x 7mm x 7mm in size, placed in between an input coupler ($R = 95\%$ for signal wavelength, highly transparent for pump and idler waves) and an output coupler ($R = 70\%$ for signal wavelength, highly transparent for pump and idler waves). The cavity length is minimized to 2.5 cm, which corresponds to a free-spectral range of 6 GHz. This is necessary to obtain as many roundtrips as possible during the temporal width of the pump pulse and, as such, driving the POPO into saturation. This results in stable output power. Moreover, when the mode spacing in the cavity of the amplifier is large, it is easier to maintain single-mode operation. An advantage of the power oscillator is that it acts as a spectral filter as well, since its free spectral range (FSR) differs from that of the GIOPO. The GIOPO has a FSR of 1.9 GHz, so if multi-mode operation occurs, the side modes are separated 1.9 GHz from

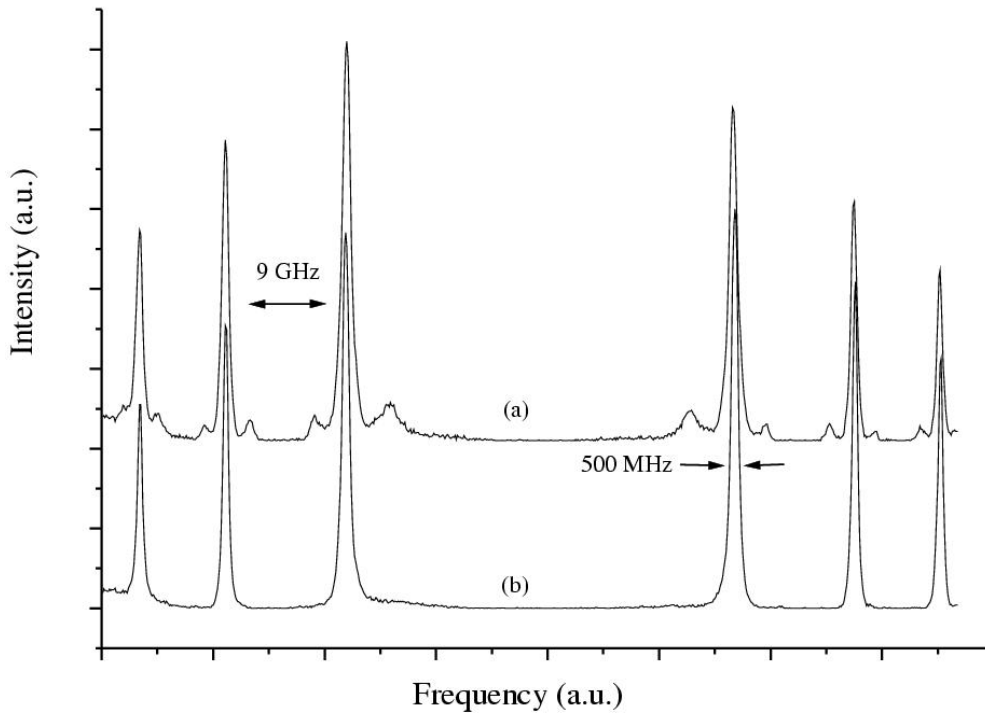


Figure 2.2: *Fabry Perot spectrum of GIOPO(a) and POPO(b) the FP interferometer has a FSR of 9 GHz and a finesse of 20. The FWHM of the POPO pulse is 500 MHz. It is clearly seen that the side modes of the GIOPO are not amplified in the POPO*

the main mode. If the POPO is locked on the main mode of the GIOPO, these side modes do not fit into the POPO cavity and will not be amplified (see fig.2.2). The POPO delivers 3 mJ output pulses of 1.5 ns at a pump energy of 11mJ (efficiency 27%).

Seeding is most efficient when the seed pulse reaches the POPO slightly before the pump pulse. The pump pulse to the POPO is delayed 1 ns with respect to the seed pulse generated in the GIOPO. The cavity length of the POPO is adjusted with a piezo electric transducer, so that the mode of the GIOPO fits inside the POPO cavity. Hence, the POPO will oscillate on exactly the same wavelength as the GIOPO. Due to the partial transmission of the input coupler of the POPO ($T = 5\%$) for the resonating light, some light leaks out of the cavity towards the GIOPO. To avoid that the light generated in the POPO disturbs the single mode operation of the GIOPO, the distance between the two oscillators is chosen longer than the length of the generated pulse.

The spectral structure and the relative frequency of the GIOPO and POPO are monitored on a home-built spectrum analyzer, which consists of a CCD camera (Pulnix TM6AS) mounted behind a 9 GHz air-spaced Fabry-Perot interferometer. In fig. 2.2 typical frame-grabber pictures of the mode structure of the GIOPO (a) and POPO (b) are given. Single

mode operation of the GIOPO-POPO combination is controlled by this spectrum analyzer and a feedback program written in a combination of C++ and Labview languages.

When the GIOPO is well aligned, it runs more or less single-mode (≤ 2 small side modes), the software determines the positions of the peaks of the spectrum analyser and the center of mass of the peaks belonging to one etalon order. Next, the positions of the side peaks are determined. A suitable voltage for the piezo mounted on the end-mirror is calculated to change the cavity length in order to suppress these side modes. Then the length of the POPO cavity is adjusted as well so that the mode of the GIOPO matches precisely this length. The spectrum analyser fringes of the POPO will show up at the same position as those of the GIOPO. In this condition, the seeding will work efficiently and the POPO will oscillate on a single longitudinal mode. However, it is essential that the alignment of the POPO with respect to the spatial distribution of the seed beam and the generated beam is perfect, otherwise single-mode operation can not be achieved.

The absolute wavelength of the POPO is measured by a wavelength meter (type ATOS Lambdameter LM-007). This wavelength meter consists of a temperature-stabilized monolithic quartz block containing four neon-filled Fizeau interferometers with different FSR's. This system can measure wavelengths between 400 and 1100 nm, with an accuracy of 0.003 cm^{-1} . A small fraction (1%) of the light from the GIOPO and the POPO is coupled into single-mode fibers and used for analysis. The light from the POPO is split into two parts, one part for to the spectrum analyser, the other part for to the Lambdameter to measure the wavelength of the device. When the measured wavelength is different from the "lock-wavelength", software calculates the desired shift in the positions of the spectrum analyser fringes (of GIOPO and POPO). From this shift the applied voltage to the different piezo's is subsequently calculated. Scanning of the device is achieved in a similar way, the "lock-wavelength" is now shifted step by step under computer control. The wavelength and Fabry Perot spectra could be measured only in the visible region due to the coupling fiber used and the etalon coating. To determine the infrared idler wavelengths generated in the OPOs, the software calculates the wavelength of the infrared idler wave from a measurement of the signal wavelength and the wavelength of the second harmonic of the pump laser. From this the wavelength of the third harmonic –the pump wavelength– follows, as well as the idler wavelength. The system has a high intrinsic stability; without active stabilization the GIOPO-POPO system is single-mode for minutes, the actively stabilized system is single-mode and drifts no more than 200MHz for hours.

The output wavelength range of the system can be further expanded by second harmonic generation. By collimating the POPO output into two BBO crystals cut at 55° in a walk-off

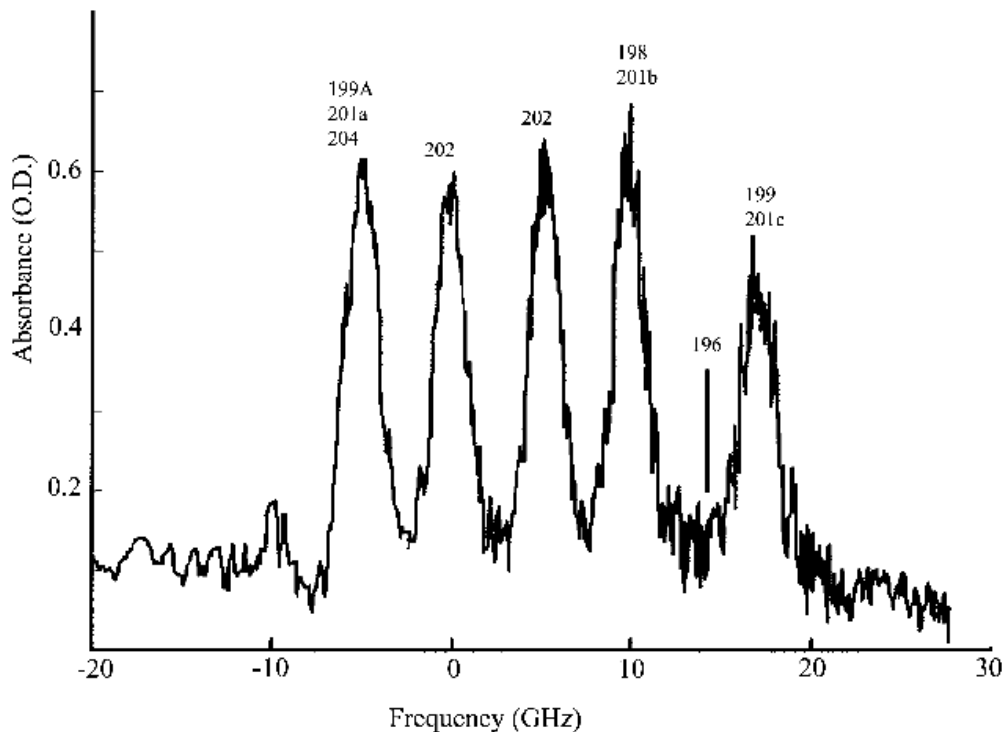


Figure 2.3: Absorption spectrum of Hg vapour at 253.7 nm.

compensated setup *e.g.*, 750 μJ UV light was generated with 3.2 mJ at 474 nm.

2.4 Applications

This OPO-device is a versatile tool for spectroscopic experiments because of its wide wavelength tuning range and narrow bandwidth. This is demonstrated here with two different types of experiments. Firstly, the resonance transition of the Hg atom at 253.7 nm was measured. For the transition from the groundstate to the first excited state, the output of the POPO -oscillating at 507 nm- was frequency doubled to generate wavelengths around 253.7 nm. The mercury is heated in a cell to a pressure of 200 mTorr. A direct absorption experiment was performed. A small part of the light was used to monitor intensity fluctuations. The length of the optical path through the vapor is 1 meter. The absorption and intensity fluctuations were measured with two identical photodiodes. The OPO system was scanned over 40 GHz. In fig. 2.3 a measured spectrum is shown, the absorption peaks for the different mercury isotopes are clearly resolved.

To test the capabilities to scan in the infrared wavelength range, a Cavity Ring Down (CRD) absorption experiment [9],[10] was performed on carbon dioxide (CO_2) at 1528 nm. CO_2 has many -weak and strong- vibrational transitions in this wavelength range. The cavity

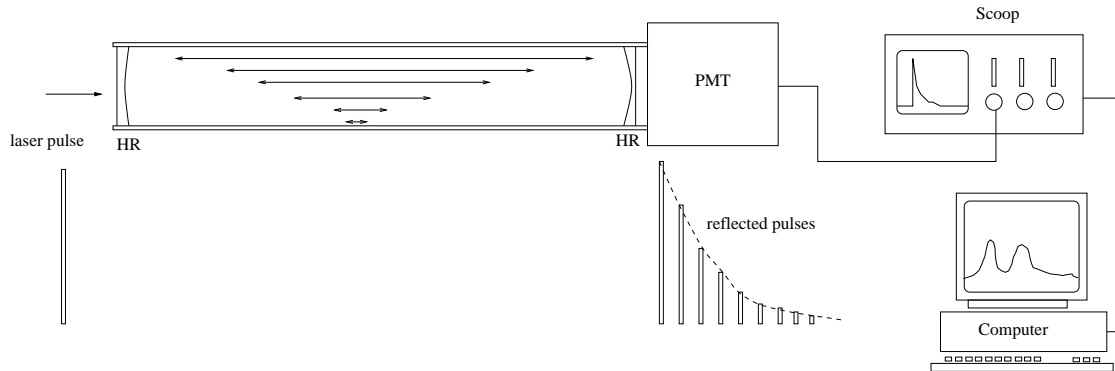


Figure 2.4: Cavity ringdown setup. HR: high reflecting mirrors coated for 1550 nm, PMT: photo multiplier.

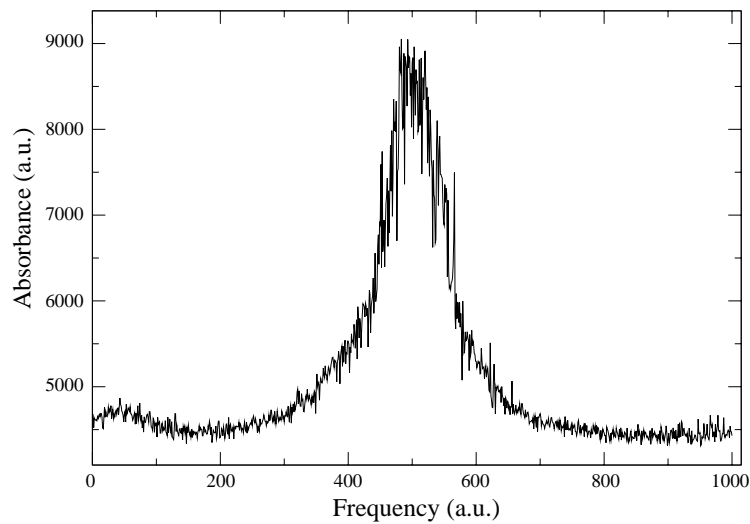


Figure 2.5: Cavity ringdown measurement of the 6543.924 cm^{-1} transition of CO_2 . The halfwidth of the peak is 0.033 cm^{-1} .

mirrors used for this experiment have a radius of curvature of 1 meter and a reflectivity of 99.99%. The cavity decay transient was detected by a high speed InGaAs photodiode with a spectral response in the range 800-1800 nm and a rise-fall time of 5 ns. The decay time of the empty cavity was measured to be $7.5 \mu\text{s}$. In figure 2.4 a CO_2 absorption line at 6543.924 cm^{-1} is shown, measured at a pressure of 76.1 Torr in the cavity. The absorption cross section of this line is $0.24 \times 10^{-6} \text{ atm}^{-1} \text{ cm}^{-2}$. On the left another transition (at 6544.075 cm^{-1}) is visible; this line has a strength of $0.15 \times 10^{-6} \text{ atm}^{-1} \text{ cm}^{-2}$.

2.5 Conclusion

In conclusion, we have demonstrated an efficient tunable SLM OPO system, that can be electronically scanned over 2.5 cm^{-1} . This scanning range can be expanded by mounting the tuning mirror on a piezo stack with a larger expansion, or by the use of a picomotor. This device is, as demonstrated, widely applicable in spectroscopy. However, the use of a SLM pump laser is prerequisite for SLM operation of the OPO-system.

The authors wish to thank Dr. B. van Oerle and J. Offerein for their assistance in the spectroscopic experiments and acknowledge the “Technologie Stichting STW” for financial support.

Bibliography

- [1] V.G. Dimitriev, G.G. Gurzadyan and D.N. Nikogosyan in ”*Handbook of Nonlinear optical Crystals*” 3rd rev. edition. A.E. Siegman, ed. (Springer, New York, 1992) Vol **64**, 345.
- [2] A. Borsutzky, “Frequency control of pulsed optical parametric oscillators” *Quantum Semi-class. Opt.* **9**, 191 (1997).
- [3] J.M. Boon-Engering, W.E. van der Veer, J.W. Gerritsen, E.A.J.M. Bente and W. Hogervorst, “Bandwidth studies of an injection-seeded β -Barium Borate optical parametric oscillator” *Opt. Lett.* **20**, 330 (1995).
- [4] Feature Issue on Optical Parametric Devices, *J. Opt. Soc. Am. B* **12** (1995) volume II.
- [5] W.R. Bosenberg, D.R. Guyer, “Single frequency optical parametric oscillator” *Appl. Phys. Lett.* **61**, 387 (1992).
- [6] L.A.W. Gloster, I.T. McKinnie, Z.X. Jiang and T. King, J.M. Boon-Engering, W.E. van der Veer and W. Hogervorst, “Narrowband $\beta - BaB_2O_4$ optical parametric oscillator in a grazing incidence configuration” *JOSA B.* **12**, 2117 (1995).
- [7] M. G. Littman and H. J. Metcalf, “Spectrally narrow pulsed dye laser without beam expander” *Appl. Opt.* **17**, 2224 (1978).
- [8] E.G. Loewen, M. Neviere and D. Maystre, “Grating Efficiency Theory as it applies to Blazed and Holographic Gratings” *Applied optics* **16**, 2711 (1979).
- [9] A. O’Keefe and D.A.G. Deacon, “Cavity ring-down optical spectrometer for absorption measurements using pulsed laser sources” *Rev. Sci. Inst.* **59**, 2544 (1988).
- [10] H. Naus, S.J. van der Wiel and W. Ubachs, “Cavity ring-down spectroscopy on the $b^1\Sigma_g^+ - X^3\Sigma_g^-(1,0)$ band of oxygen isotopomers” *J.Mol. Spectr.* **192**, 162 (1998).

Chapter 3

Travelling-wave nanosecond Optical Parametric Oscillator close to the Fourier-transform limit

3.1 Abstract

We report on a novel design for a nanosecond Optical Parametric Oscillator (OPO) based on beta-barium-borate (BBO). It involves a travelling-wave ring cavity in a configuration with a grazing incidence grating. This OPO is pumped by the third harmonic of multi-mode as well as a single-mode Nd:YAG lasers. The observed bandwidth of 0.5 GHz at a pulse duration of 1.3 ns when pumped with the single-mode laser is close to the Fourier-transform limit. A numerical evaluation of an equivalent standing-wave cavity shows a frequency shift for the resonant wave due to an induced non-linear index of refraction .

3.2 Introduction

One of the important performance criteria for pulsed, nanosecond optical parametric oscillators (OPOs), in particular in e.g. lidar applications and photo-acoustic spectroscopy [1] [2], is how close the Fourier-transform limit, characterized by the product of spectral bandwidth and pulse duration, is approached. Among the various techniques to narrow the OPO bandwidth (see review in ref. [3]) the use of a grazing-incidence (GI) grating has been demonstrated successfully [4]. Even single longitudinal mode (SLM) operation is feasible. In a GIOPO device the favourable intrinsic properties of a nonlinear crystal can be exploited optimally as far as the tunability over a wide spectral range is concerned. SLM operation and a large scan range have been demonstrated with a GIOPO based on a beta-barium-borate (BBO) crystal, covering a signal range from 460 to 630 nm [5].

In comparison with the alternative technique of bandwidth narrowing by injection seeding of a pulsed OPO [2], [6], the GI grating configuration appears to be potentially more cost-effective as it does not require a series of CW single-mode seed sources to cover a wide

tuning range. Further improvements of GIOPOs, such as new cavity designs and pump geometries, however, are desirable. Recently, periodically-poled nonlinear crystals have been successfully used as well for SLM-GIOPOs [7].

In this paper, we report on what is, to our knowledge, the first demonstration of bandwidth narrowing and SLM operation close to the Fourier-transform limit for a GIOPO based on a travelling rather than a standing wave cavity. In general, according to a model of bandwidth narrowing in the limit of low pump depletion [8], which is appropriate for pulsed GIOPOs, the spectral composition follows from a convolution of the bandwidths defined by the nonlinear crystal as well as by the grating. The resulting bandwidth is dominated by the grating contribution, which involves a sum of diffraction and aperture terms. The diffraction term decreases with a shorter cavity, and increases with the GI-angle. The aperture term is proportional to the pump beam diameter and decreases with an increased GI-angle and the number of round trips inside the cavity. Obviously, bandwidth narrowing through shortening the cavity has its technological limit. Also a decrease in the diameter of the pump beam usually results in unfavourable spatial walk-off between parametric and pump beam.

This walk-off can be successfully compensated in non-collinearly pumped OPO configurations [9]. However, it requires simultaneous rotation of the non-linear crystal and the cavity axis with respect to the pump beam. In addition to an increased device complexity it results in significant changes in the directions of the parametric output beams.

Attractive simplicity is achieved in a device with a forward-backward pump configuration [10], and using this walk-off self-compensation. This results in a decrease of the threshold pump energy of the OPO as well. Nevertheless, such a double-pass pump configuration increases the risks of crystal damage and causes other undesired effects originating from the overlapping of the pump beams [8], [11]. Walk-off compensation was also automatically achieved in a free-running ring-cavity OPO with two spatially separated regions for the parametric interaction in a crystal pumped from opposite directions [12] [13]. A similar solution is applied in our present work on a narrow bandwidth OPO. In these approaches the use of an additional tuning mechanism based on a synchronous mutual rotation of non-linear crystals, used to compensate walk-off in some practical OPO devices [14], can not be applied.

Bandwidth narrowing down to the SLM regime by increasing the GI-angle on the grating is accompanied by considerable reduction of grating efficiency and results in higher intracavity losses and an increased oscillation threshold. At higher pump fluences the oscillation spectrum of the nanosecond OPOs will be altered by backconversion of signal and idler waves into pump light [6] as well as by frequency chirp [15]. Such spectral features will be most pronounced in standing-wave cavities, where a phase mismatch may occur as a conse-

quence of changes in the index of refraction induced by constructive optical interference, in particular in the case of overlapping, counter propagating pump pulses.

Nevertheless, for a double-pass pump beam with a fixed duration of the initial pulse further bandwidth narrowing and reduction of the threshold are possible by increasing the effective number of cavity round trips of the parametric waves. This requires that the initial and return passes are separated in time by an appropriate delay time corresponding to at least about one-half of one full-width at half-maximum (FWHM) intensity of the pump pulse [16]. In any case, a solution of the problem of spectral narrowing implies a reasonable trade-off between the attainable bandwidth and the losses introduced. Considering these aspects as well as the unidirectional nature of parametric gain, led us to the approach of a travelling-wave GIOPO based on a compact ring cavity.

3.3 Experimental setup

A schematic of our experimental setup is shown in fig. 3.1. The ring cavity contains an end-prism, a diffraction grating and a tuning prism. A BBO crystal, cut for type-I phase matching ($e \rightarrow o + o$), and a pump steering mirror are mounted between the end-prism and grating. The dispersion plane of the grating is parallel to the extraordinary plane of the crystal. Other types of phase matching may also be used in this configuration. Both prisms are 90° and act as retroreflectors that fold and displace the relevant light beams. The steering mirror is a high reflector for 355-nm pump light at 45° angle of incidence with s-polarization, with a specified damage threshold of 230 MW/cm^2 for an 8 ns pulse, and has a transmittance $T > 90\%$ in the region 430-680 nm for a resonated parametric signal wave of p-polarization. Due to its inclined mounting this mirror will in fact sustain pump fluences up to 325 MW/cm^2 . The steering mirror serves to direct the pump beam into the cavity and to couple out the depleted pump radiation. The end-prism and the steering mirror form a pump beam in the crystal for two spatially separated regions of parametric interaction, with parallel optical axes.

The new element in this configuration (the 'tuning unit' in Fig.1) is a specific combination of tuning prism and grating. For high spectral dispersion the grating is mounted at GI relative to a parametric wave, generated in a particular region of the crystal (Littman configuration [17]). The OPO signal and idler output are coupled out via the specular (zeroth order) reflection on the grating (Fig.1b). The diffracted parametric signal beam is folded in the tuning prism, arranged in an appropriate resonant position. But in contrast to

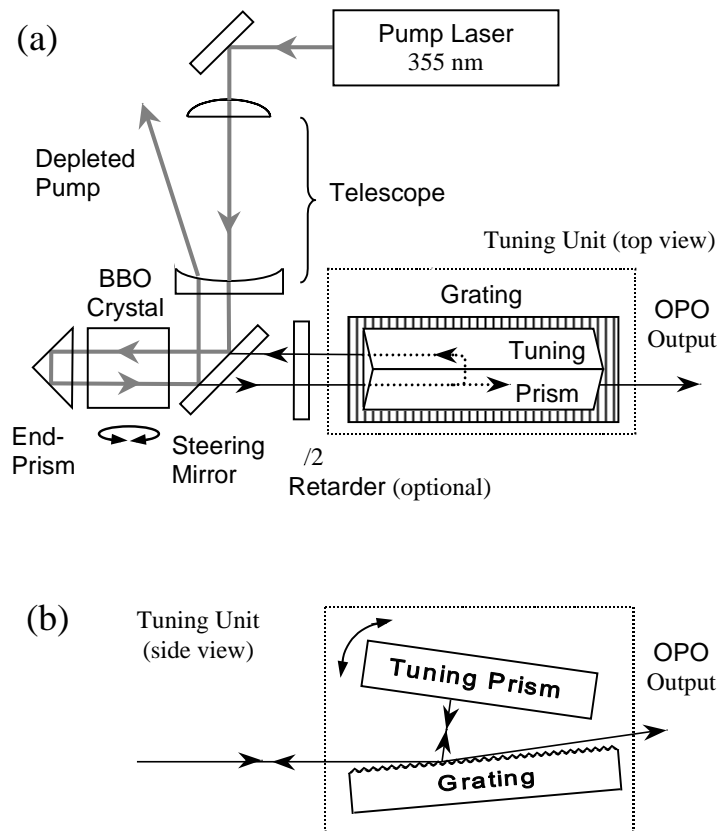


Figure 3.1: Schematic of the GIOPO set-up: (a) Top view of ringcavity formed by the end prism and tuning unit, containing a grating and tuning prism, $\lambda/2$ retarder is removed when a grating with enhanced s-polarisation efficiency is used. (b) Side view of the tuning unit; the grating is arranged in a grazing incidence configuration, the zero order reflection on the grating gives the OPO output.

the conventional case of a tuning mirror, this beam is additionally displaced by the tuning prism and is reflected back to the grating in spatially shifted position. It is reflected again on the grating at GI back to the steering mirror, propagates through this mirror and the second pumped region in the crystal, reaches the end-prism and after folding and displacement the round trip is closed. Fine wavelength tuning is achieved by tilting the tuning prism in the dispersion plane of the grating. In the present study we did not focus on options for a smooth, mode-hop-free tuning [18].

The 90° prisms are made of fused quartz. Total internal reflection at the uncoated base facets is used. To construct a compact cavity the prism hypotenuse facet is chosen of the same size as the crystal aperture. The length of the tuning prism is about equal to the length of the exposed area on the grating (5 cm). Appropriate broadband antireflection (AR) coatings are used on the hypotenuse facets. In principle, for better stability in single-mode operation, it is possible to replace the prism by a double-mirror, hollow retro-reflector

to eliminate unwanted differences in phase shifts occurring during total internal reflection of pump and parametric waves. Total phase shifts for the signal wave at 458 nm and the idler wave at 1578 nm e.g. accumulate to -1.88 rad and -1.57 rad, respectively, whereas for the 355-nm pump wave the shift is -1.13 rad. Furthermore, when this retro-reflector is coated such that it is transparent for the idler wave, the idler will escape from the cavity at each pass through the crystal, thus limiting the back-conversion into the pump wave [19]. In contrast to the end-prism, the tuning prism only manipulates the single resonated parametric wave and does not significantly affect phase conditions. In comparison with a standing wave OPO [20], in the equivalent travelling wave configuration the total number of Fresnel reflections at crystal faces and the steering mirror per round trip is halved. It allows for the use of an uncoated BBO crystal, which has a surface damage threshold in the order of 500 MW/cm² for a 355-nm pump pulse with a 10 ns duration [21].

3.4 Results

The experiments were performed with three types of frequency-tripled, pulsed nanosecond Nd:YAG lasers: multi-longitudinal mode, multi-mode, and single-longitudinal-mode. The first laser (home-built) was a nearly diffraction limited multi-longitudinal mode pump laser with a maximum pulse energy of 18 mJ and duration of 8 ns. An uncoated BBO crystal (cross section 6 mm x 6 mm, length 10 mm) was used cut at $\Theta = 30^\circ$ with respect to the crystal axis. The geometrical cavity length was 8 cm, corresponding to a free spectral range (FSR) of 1.8 GHz. The pump beam was well-collimated down to a diameter of 1 mm using the variable telescope shown in Fig.1. The depleted pump beam was removed from the cavity and is not retro-reflected back into the pump laser. A commercially available, replicated ruled grating with 1800 grooves/mm and enhanced s-polarization efficiency near 500 nm (State Optical Institute, RU) was used. This type of so-called "very-high-blaze-angle" grating [22] well matches the relevant polarization conditions. Therefore, the $\lambda/2$ retarder (Fig.1a) was not inserted. At a GI-angle of about 880 the spectral bandwidth of the resonated (signal) wave at 500 nm was narrowed down to 3.6 GHz (0.12 cm^{-1}), while in a common standing-wave cavity at the same GI-angle oscillation threshold was not even reached. Then reliable output was only observed at a GI -angle of 87° with a bandwidth of 30 GHz. SLM parametric oscillation could not be achieved because of the multi-longitudinal mode structure of the pump laser. This is in agreement with observations by Baxter et al [23], who varied the bandwidth of their pump laser from SLM oscillation to several tens of GHz. In the latter case this resulted in an OPO operating on multiple modes.

It must be emphasized, that the coplanarity of the dispersion plane of the grating and the extraordinary plane of the crystal gives an optimal configuration for a ring GIOPO. In addition it also contributes to bandwidth narrowing. Indeed, in a slightly modified version of the model for the bandwidth narrowing the proportionality between spectral and angular bandwidths is considered [24]. When the acceptance angle of the nonlinear crystal in the extraordinary plane is taken into account, it follows that the resulting angular spectra are determined by a convolution of the corresponding angular distribution with the acceptance angle contour. Then a crystal with a small acceptance angle (such as e.g. BBO) functions additionally as an intrinsic spatially-spectral filter. In ref. [24], such a condition is called an extraordinary resonance.

Unfortunately, the "very-high-blaze-angle" grating does not allow a wide range of tunability, because its efficiency for s-polarization is higher than for p-polarization only in a narrow spectral range. Therefore, to investigate tuning options for our ring GIOPO this grating was replaced by a standard holographic grating with periodicity of 2400 grooves/mm and a suitable p-polarization efficiency in a wide visible range (Spectronic Instruments). A second multi-mode laser (model LQ-727, SOLAR LS) with beam propagation factor of $M^2 > 3$ and bandwidth of 30 GHz was used to pump, after collimation down to a diameter of 1.8 mm, an uncoated BBO crystal (cross section 7 mm x 7 mm, length 12 mm, cut at $\Phi = 28^\circ$). A maximum pump energy of 30 mJ/pulse was used with pulse duration of 6 ns. Now the $\lambda/2$ retarder has to be mounted in the cavity to rotate by 90° the polarization of the signal wave. At first sight, the best option for the retarder appears to be a broadband superachromatic half-waveplate operating simultaneously within the visible and near-infrared spectral ranges [25]. However, due to its large geometrical length (almost comparable with an equivalent Fresnel Rhomb) such an optical component inside the cavity will increase the device threshold significantly. Instead we inserted a retarder based on a zero-order half-waveplate (RZ-1/2-515, Optics for Research) specified at $\lambda = 515$ nm, i.e. near the centre of the desired spectral range for the signal wave. An AR coating provides a total $T > 98\%$ within a bandwidth of ± 6 nm (i.e. the wavelength tolerance on either side of the central wavelength, over which the retardation is within $90^\circ \pm 10^\circ$). We observed relatively smooth tuning of the signal output in the spectral range 450 - 650 nm with a maximum total efficiency of 4% at a pump energy of 21 mJ. The oscillation threshold was measured to be 12 mJ (80 MW/cm^2) at 505 nm at a GI-angle of 87° . The upper limit of the signal bandwidth measured with a Fabry-Prot etalon was 30 GHz (1cm^{-1}), equal to that of the pump laser. The tuning range was covered by tilting the tuning prism and rotating the crystal without any change of optics. Grating reflectivity and some mechanical design constraints were found

to be the factors limiting the tuning range. So even far beyond the narrow retardation range of ± 6 nm around 515 nm, the polarization component of the signal in the extraordinary plane is sufficiently strong to overcome the extra losses. The design shows a relatively low threshold for a pump beam with high M^2 and it can be a good option for a master oscillator in a system with a second stage of power amplification for middle-resolution applications.

The resonated wave of an OPO can be significantly narrowed when pumped with a broadband laser if the non-resonant wave is allowed to carry away the excess bandwidth [26]. This is the case e.g. in a continuous-wave SLM OPO based on a periodically poled crystal in a four-mirror ring cavity pumped by a nearly diffraction limited beam ($M^2 = 1.1$) with a bandwidth comprising several longitudinal modes [27]. However, in general this will not work in a nanosecond OPO system, where a SLM pump laser is required for SLM operation. For this reason we also used a SLM pump with a spectral bandwidth of 0.25 GHz, a pulse duration of 3 ns and a maximum energy of 14 mJ at repetition rate of 20 Hz (Coherent Infinity 40-100). The variable telescope (fig.1a) was replaced by a relay imaging system to form a beam profile with reduced intensity inhomogeneity and an average diameter of 2.3 mm. SLM operation of our ring OPO was observed at a GI-angle of 89.5° , with an oscillation threshold of only 11 mJ/pulse (88 MW/cm²). The cavity FSR is 1.9 GHz, corresponding to only 5-6 round trips. No scheme for stabilization of the cavity was used. Three measurements of the OPO bandwidth recorded with a FPI are shown in fig. 3.2. SLM oscillation was achieved within the wavelength range of ± 5 nm centered at 515 nm, defined by the total bandwidth of the $\lambda/2$ retarder. Traces (a) and (c) correspond to the boundaries of this range and indicate the appearance of 2-3 additional modes. An appropriate increase in effective duration of the pump pulse and hence, in the number of round trips, may allow for more extensive single-mode tuning. Trace (b) shows a representative etalon signal of SLM oscillation at 515 nm with an instrument-limited optical bandwidth (FWHM intensity) of 0.5 GHz, averaged over ten pulses. Side lobes of low intensity near the SLM peak can be attributed to mechanical instabilities of the cavity and to a difference in phase shifts at internal reflections in the end-prism. Figure 3.3 shows the temporal profile of the SLM output signal at 515 nm, again averaged over ten detected pulses and displayed on a digital oscilloscope. The pulse duration (FWHM intensity) is 1.3 ns. Together with the measured value of the SLM bandwidth it yields a product of spectral bandwidth and pulse duration of 0.65, which is close to the Fourier-transform limited value of 0.44 for a Gaussian pulse. For comparison, the product for the pump laser used in the experiment is 0.75. Typical values for this product for nanosecond OPOs are 2-4 times larger than the Fourier-transform value [1],[4].

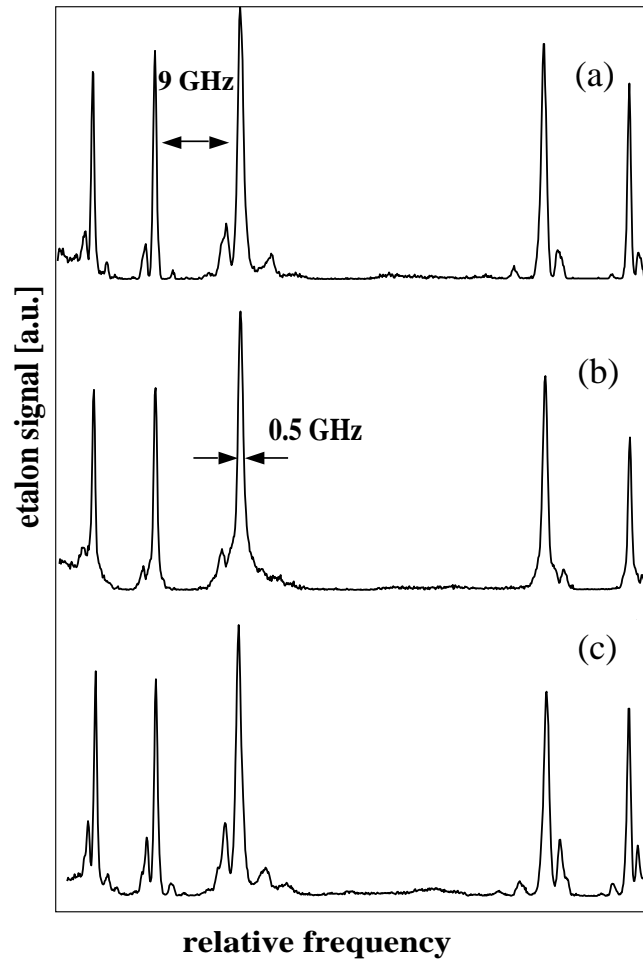


Figure 3.2: Intensity profiles at the centre of the fringe pattern formed by a 9 GHz FSR Fabry-Perot interferometer (FPI). The traces correspond to the SLM pumped OPO operating at wavelengths of (a) 501 nm, (b) 515 nm and (c) 520 nm. The bandwidth of the pulses is 0.5 GHz, averaged over 10 pulses.

3.5 Discussion

A bandwidth in excess over the Fourier-transform limit indicates the presence of some amplitude or phase substructure in the pulse that may result in frequency chirp. This is commonly induced by time-dependent as well as spatially dependent changes in the index of refraction. In an equivalent standing-wave GIOPO configuration with self-overlap of the

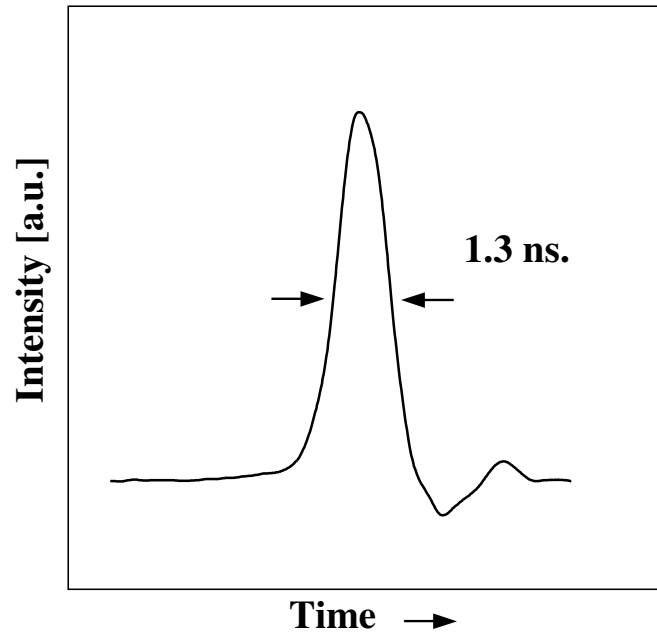


Figure 3.3: Temporal profile of the OPO output at 515 nm detected with a fast photodiode and averaged over 10 pulses. The pulse duration (FWHM) is 1.3 ns. The duration of the pump pulse is 2.5 ns.

incident and back reflected pump beam [12], these changes can be more pronounced due to the superposition of the beams. When the pump pulse with frequency bandwidth interacts with another identical pulse, delayed by a time $\Delta\tau$, the visibility of the interference pattern is given by [28]

$$\frac{e^{(-\pi\tau\Delta\nu)^2}}{4\ln 2}. \quad (3.1)$$

Specifically, for an almost undepleted pump beam and typical values $\Delta\nu = 0.25$ GHz and $\Delta\tau = 0.1$ ns used in the experiment with the Coherent Infinity SLM pump laser, the fringe visibility in such a standing-wave configuration is high and exceeds 97%. Then the resulting intensity distribution along the optical axis x may be approximated as:

$$I(x) = 4I\cos^2(kx), \quad (3.2)$$

where I is the peak intensity of the incident pump pulse with wave number \vec{k} . In the pump field of intensity $I(x)$ the refractive index is described to first order as

$$n(x) = n_0 + n_2I(x), \quad (3.3)$$

where n_0 is the linear term of the index of refraction and n_2 the nonlinear term related to the second-order susceptibility of the nonlinear crystal. Substituting 3.2 into 3.3 gives

$$n(x) = n_0 + 4In_2\cos^2(kx). \quad (3.4)$$

Since the period of the fringe pattern is much shorter than the crystal length L , averaging 3.4 over x results in $n = n_0 + 2In_2$. Consequently, the induced component of the refractive index is:

$$n - n_0 = 2In_2. \quad (3.5)$$

When a possible wavelength dependence of this component is neglected for a singly resonant beam with wavelength λ the added phase shift per round trip then becomes:

$$\Delta\Phi = \frac{4\pi L(n - n_0)}{\lambda}. \quad (3.6)$$

For a round trip time δt this shift is equivalent to a frequency change of $\delta\nu = \Delta\Phi/\delta t$ [29]. Substituting 3.5 into 3.6 gives the following expression for the corresponding frequency change:

$$\delta\nu = \frac{8\pi n_2 I L}{\lambda \delta t}. \quad (3.7)$$

For values of the parameters for a BBO crystal for a typical OPO, $n_2 = 2.910^{-16} \text{cm}^2/\text{MW}$ [29], $L = 12 \text{ mm}$, $\lambda = 515 \text{ nm}$, $I = 88 \text{ MW/cm}^2$ (at threshold) and $\delta t = 0.5 \text{ ns}$ (measured from the cavity FSR) expression 3.7 yields $\delta\nu = 300 \text{ MHz}$, which is comparable to the typical value for the bandwidth of a few hundred MHz for a GIOPO output. The evaluation of an effect of the resonant parametric wave on the frequency shift as well requires a more rigorous model. This is the subject of a future study.

3.6 Conclusion

We have demonstrated a travelling-wave nanosecond GIOPO operating close to the Fourier-transform limit for a Gaussian pulse. An improvement in the spectral quality of a nanosecond GIOPO has been demonstrated in a setup where a standing-wave distribution of intensities is avoided. This is analogous to the improved bandwidth observed in active laser systems when 'spatial hole burning' effects are eliminated in a travelling-wave ring structures. A standing-wave OPO configuration also may give additional frequency shifts, as shown, caused by

the phase mismatch induced by a nonlinear index of refraction, related to the second-order susceptibility of the crystal. In addition, our configuration of a frequency-selective ring cavity is compact and walk-off compensated with a relatively low threshold. It may serve as a master oscillator in practical devices for high-resolution applications [31], [32]. Our optical lay-out completely eliminates any unwanted return of pump and parametric light into the pump source.

Bibliography

- [1] G.W. Baxter, H.-D.Barth, B.J.Orr, *Appl. Phys. B* 66 (1998) 653.
- [2] G. Ehret, A.Fix, V.Weil, G.Poberaj, T.Baumert, *Appl. Phys. B* 67 (1998) 427.
- [3] A. Borsutzky, *Quantum Semiclass. Opt.* 9 (1997) 191.
- [4] W.R. Bosenberg, D.R. Guyer, *Appl. Phys. Lett.* 61(1992) 387.
- [5] J.M. Boon-Engering, W.E. van der Veer, E.A.J.M. Bente, W. Hogervorst, *Opt. Commun.* 136 (1997) 261.
- [6] A.V. Smith, W.J. Alford, T.D. Raymond, *J. Opt. Soc. Am. B* 12 (1995) 2253.
- [7] P. Schlup, G.W. Baxter, I.T. McKinnie, *Opt. Commun.* 176 (2000) 267.
- [8] S.J. Brosnan, R.L. Byer, *IEEE J.Quantum Electron.* 15 (1979) 415.
- [9] L.A.W. Gloster, I.T. McKinnie, T.A. King, *Opt. Commun.* 112 (1994) 328.
- [10] L.R. Marshall, A.D. Hays, J.J. Kasinski, R. Burnham: *Adv. Solid State Lasers*, Salt Lake City, UT (OSA Washington, DC, March 1990) Postdeadline paper WC8PD-2.
- [11] B.C. Johnson, V.J. Newell, J.B. Clark, E.S. McPhee, *J. Opt.Soc.Am. B*12(1995) 2122.
- [12] Yu.N. Belyaev, A.M. Kiselev, G.I. Freidman, *Izvestia Vischikh Utchebnikh Zavedenii (USSR), Radiofizika*, 14 (1971) 1182.
- [13] E. Margalith, US Patent No 5.276.548, 1/1994.
- [14] W.R. Bosenberg, US Patent No 5.047.668, 9/1991.
- [15] D.C. Hovde, J.H. Timmermans, G. Scoles, K.K. Lehmann, *Opt. Commun.* 86(1991)294.
- [16] C.David Nabors, US Patent No 5.786.929, 1/1998.
- [17] M.G. Littman, H.J. Metcalf, *Appl. Opt.* 17 (1978) 2224.
- [18] L. Nilse, H.J. Davies, C.S. Adams, *Appl. Opt.* 38 (1999) 548.
- [19] W.J. Alford, A.V. Smith, US Patent No 6.147.793, 11/2000.
- [20] W.R. Bosenberg, W.S. Pelouch, C.L. Tang, *Appl. Phys. Lett.* 55 (1989) 1952.
- [21] H.Kouta, *Appl. Opt.* 38 (1999) 545.
- [22] *The Photonics Design and Applications Handbook* (Lauring Publishing Co., Inc., Pittsfield, MA, 1996) 406.

-
- [23] G.W. Baxter, P. Schlup, I.T. McKinnie, *Appl. Phys. B* 70 (2000) 301.
 - [24] B.L. Harlamoff, J.J. Jacob, US Patent No 5.406.409, 4/1995.
 - [25] P.Hariharan, *Meas. Sci. Technol. (UK)* 9 (1998) 1678.
 - [26] J.M. Boon-Engering, L.A.W. Gloster, W.E. van der Veer, I.T. McKinnie, T.A. King, W. Hogervorst, *Opt. Lett.* 20 (1995) 2087.
 - [27] W.R. Bosenberg, A. Drobshoff, J.I. Alexander, L.E. Myers, R.L. Byer, *J. Opt. Soc. Am.* 21 (1996) 1336.
 - [28] W. Koechner, *Solid state laser engineering* (Springer, Berlin, 1999), chapter 5.
 - [29] A. Siegman, *Lasers* (University Science Books, Mill Valley CA, 1986), chapter 29.
 - [30] R. De Salvo, A.A. Said, D.J. Hagan, E.W. Van Stryland, M. Sheik-Bahae, *IEEE J. Quantum Electron.* 32 (1996) 1324.
 - [31] S. Wu, V.A. Kapinus, G.A. Blake, *Opt. Commun.* 159 (1999) 74.
 - [32] J. Mes, M. Leblans and W. Hogervorst, *Opt. Lett.* 109 (2002) 9772.

Chapter 4

Third-harmonic generation of a cw Ti:Sapphire laser in external resonant cavities

An all-solid-state tunable cw laser operating near 272 nm with a bandwidth $\Gamma \approx 3$ MHz has been developed. The third harmonic of light from a single cw Ti:Sapphire laser has been generated using two external enhancement cavities. An output power of 175 mW has been produced, corresponding to an overall conversion efficiency of 8%.

4.1 Introduction

All-solid-state tunable lasers are compact and reliable sources of high-power, narrow-band coherent radiation. The applicability of these lasers, however, is limited as they mainly are operational in the red and infrared part of the spectrum. The goal of the present work was to construct an all-solid-state laser system operating at deep-UV wavelengths. Solid-state UV-laser systems producing the fourth harmonic of Nd:YVO₄ are commercially available. These systems are useful for certain applications, however, their wavelength (266 nm) cannot be tuned or scanned. Development of tunable UV-lasers has been reported by the group of Hänsch, [1], [2]. Bourzeix et al. [3] reported on a fully solid-state UV-laser system, generating the fourth harmonic of a Ti:Sapphire laser. We report on third-harmonic generation of light from a tunable continuous-wave (cw) Ti:Sapphire (Ti:S) laser. This is achieved using two steps. Firstly second harmonic light is produced using an LBO crystal inside an external enhancement cavity (EEC). Subsequently this second harmonic light is coupled into a second EEC, together with the fundamental light. Here the sum frequency is generated in a BBO crystal. The power $P_{3\omega}$ generated in the sum frequency process in the BBO crystal is given by:

$$P_{3\omega} = \gamma P_{\omega} P_{2\omega} \quad (4.1)$$

Here P_{ω} and $P_{2\omega}$ are the incident fundamental and second harmonic power respectively and γ is the nonlinear coefficient of the process. Resonantly enhancing both wavelengths inside a cavity leads to a high conversion efficiency for the sum frequency process, expressed by:

$$P_{3\omega} = \gamma A_{\omega} P_{\omega} A_{2\omega} P_{2\omega} \quad (4.2)$$

A_{ω} and $A_{2\omega}$ are the cavity enhancement factors for the fundamental and second harmonic waves and now P_{ω} and $P_{2\omega}$ are the respectively powers of the light coupled into the cavity.

Sum frequency generation with two diode lasers was realized by Sayama and Ohtsu [4]. Doubly-resonant sum frequency light using two Nd:YAG lasers was generated by Kaneda and Kubota [5]. Also, by combining a Ti:S and a diode laser a narrow-band, cw UV source with several tens of milliwatts output power was designed by Fujii et al. [6]. Third harmonic generation using only a single Ti:S laser was demonstrated by Sayama and Ohtsu [7], producing 8 nW of deep UV radiation. In the present work, doubly-resonant sum frequency generation using a single Ti:S laser is demonstrated. The doubly-resonant cavity is equipped with two Brewster plates to compensate for the dispersion in the crystal. The result is a compact, narrow-band ($\Gamma \approx 3$ MHz), tunable cw laser capable of producing 175 mW of output power in the deep UV.

4.2 Experimental setup

A schematic of the setup is shown in figure 4.1. Narrow-band 817 nm light from a tunable cw Ti:S laser (Coherent 899-21), which is pumped by a 10 W Spectra Physics Millennia-X laser at 532 nm is separated into two beams using a 50/50% beam-splitter. The light of one of the beams is frequency doubled inside a bowtie-shaped EEC using a LBO nonlinear crystal cut at angles of $\theta = 90^\circ$, $\phi = 29.8^\circ$ with respect to the optical axis. The crystal is cut at Brewster's angle for the fundamental wavelength. Mode matching of the Ti:S light into the EEC

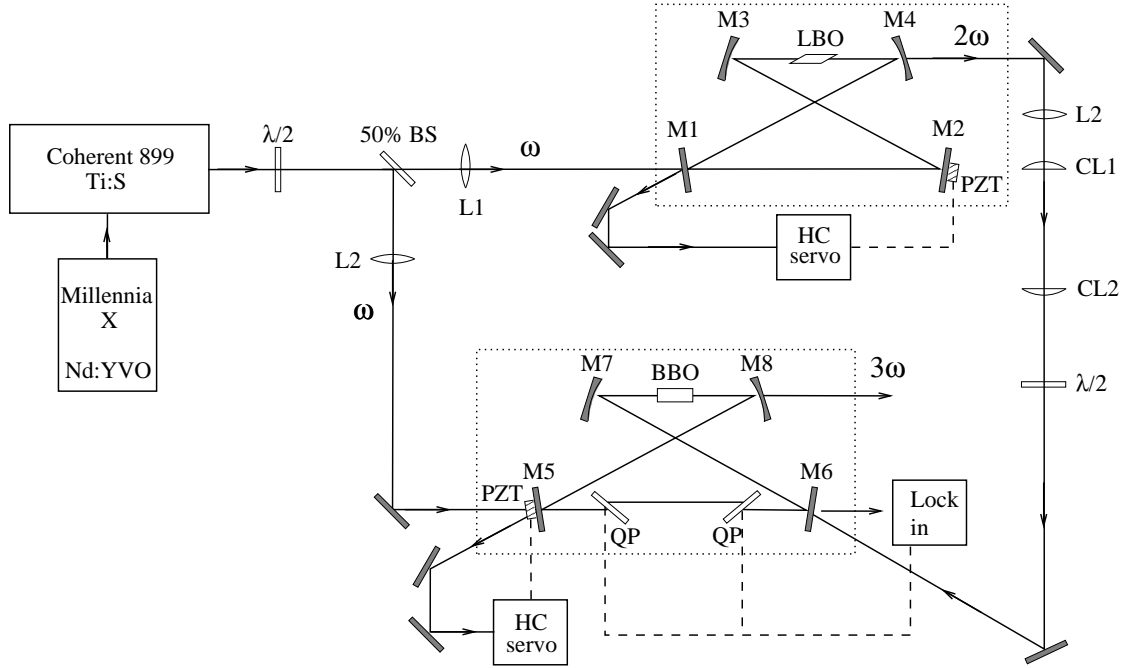


Figure 4.1: Schematic of the setup for generation of the third harmonic of a Ti:S laser. BS: beamsplitter, QP: quartz plate, PZT: piezo, L: mode-matching lens, CL: cylindrical lens, M: mirror, HC: Hänsch Couillaud locking setup.

is performed by a thin lens L1. The cavity losses per roundtrip are close to 1%, therefore the reflectivity of the input coupling mirror (M1) is chosen to be 99% to ensure impedance matching. This leads to a maximum coupling of 88% of the fundamental light into the EEC. The mirrors M3 and M4 have a reflectivity $> 99.8\%$ and a radius of curvature of -75 mm to focus the beam inside the LBO crystal. The distance between M3 and M4 is optimized for maximum conversion efficiency. To keep the EEC in resonance, the cavity is locked to the fundamental wavelength using the Hänsch-Couillaud locking technique [8] which supplies a feedback signal to the small ($\varnothing 6$ mm x 2 mm) mirror M2 mounted on a piezo-electric crystal. The second harmonic light is coupled out through M4 which is highly transparent ($> 97\%$) for the blue light at 408.5 nm.

From the FWHM of the cavity etalon peaks and the free spectral range a cavity finesse of about 530 is deduced. This leads to a cavity enhancement factor of 280, when conversion losses are not taken into account. From 1.00 W of input power at the fundamental wavelength 500 mW of usable second harmonic power is measured behind the output coupler M4, a conversion efficiency of 50%. Taking into account the second harmonic losses on the Brewster surface of the crys-

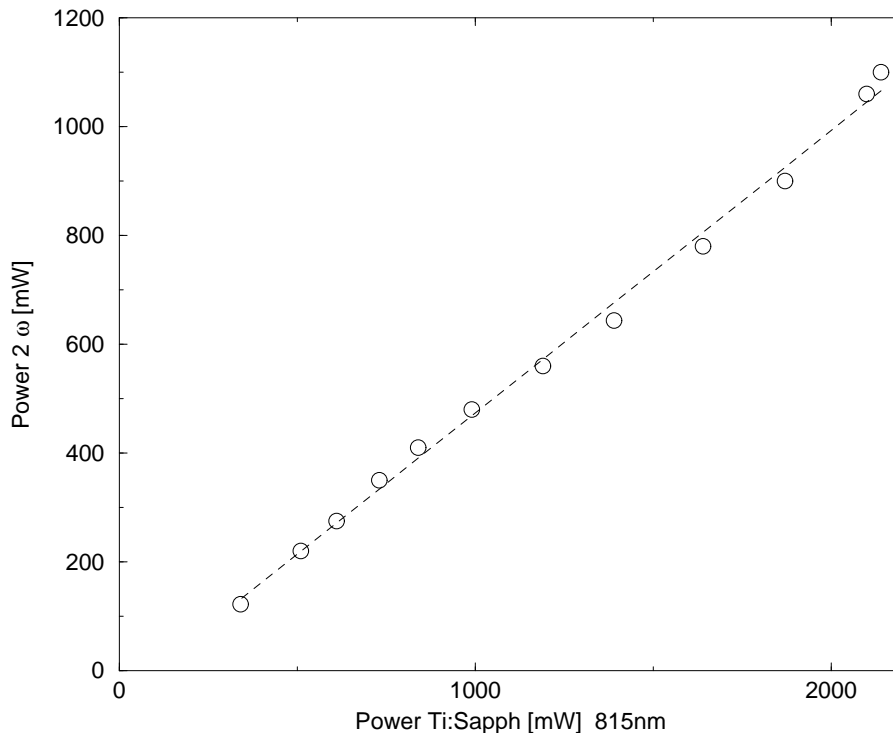


Figure 4.2: Output power of the 2nd harmonic as function of Ti:S power. The output power is measured after a dichroic mirror to separate residual fundamental and second harmonic.

tal (19.7%) and loss at M4 (2%) (Jurdik et al. [9]), this corresponds to a total conversion efficiency of 63.5%. To our knowledge this is the highest conversion efficiency up to now reported for cw frequency doubling of a Ti:S laser. Even higher conversion efficiencies (up to 85%) have been reported by the group of Kimble [10] by doubling a Nd:YAlO₃ laser to 540 nm. The output power dependence on fundamental input power of the frequency doubling system is shown in figure 4.2.

The second EEC is built up using doubly-reflecting mirrors in order to enhance both the fundamental and the second harmonic. The small (\varnothing 6 mm x 2 mm) mirror M5 mounted on a piezo is the input coupler for the fundamental, whereas M6 is the input coupler for the second harmonic. The roundtrip losses for the fundamental are close to 1%. For impedance matching the reflectivity of M5 is chosen to be 99% for the fundamental and $> 99.8\%$ for the second harmonic. On the other hand roundtrip losses for the second harmonic are about 3%, hence M6 is chosen to be 97% reflective for the second harmonic and $> 99.8\%$ for the fundamental. The mirrors M7 and M8, reflectivity $> 99.8\%$ for both

waves, have a radius of curvature of -75 mm, focusing both wavelengths inside a BBO crystal. Due to the spatial distribution of the resonator eigenmodes the waists of both wavelengths will automatically overlap inside this crystal. This significantly simplifies the alignment procedure of the EEC. Note that the waist sizes of both waves will differ by a factor of the square root of their wavelengths. The BBO crystal is cut at an angle of 42.2° and is anti-reflection-coated for all three relevant wavelengths. The third harmonic light is coupled out through M8, which is $> 95\%$ transparent at 272 nm. For the fundamental light the EEC has a finesse of approximately 310 leading to an enhancement of 98. The finesse for the second harmonic light is measured to be 63, so the enhancement is 29.

The light sent into the EEC has to be properly mode matched in order to maximize the coupling. For the fundamental this is achieved with mode matching lens L2. Mode matching the second harmonic is rather more complicated. Since the output of the second harmonic EEC is divergent and elliptically shaped, a spherical lens L3 and two cylindrical lenses CL1 and 2 are used to shape the beam profile. Lens L4 provides the mode matching for the second harmonic. For the fundamental and second harmonic 88% and 75% incoupling is achieved, respectively.

At first glance, one would expect that when the cavity is resonant with the fundamental, it is also resonant with the second harmonic. However, this is not the case. Because of dispersion in BBO the optical path lengths of the respective waves differ, giving rise to a shift from resonance of the second harmonic when the cavity is locked to the fundamental. This problem is overcome by inserting two flat quartz plates in the cavity mounted on counter rotating galvos. To minimize losses, these plates are mounted under Brewster's angle which is almost the same for both waves.

Tuning the angle of these plates leads to an optical path length difference between both waves allowing for the compensation of the dispersion in BBO. This optical path length difference is calculated to be about 200 nm when the angle is tuned over 0.1° degree for two 2 mm thick plates. Thus the cavity can be made resonant for both wavelengths: firstly the cavity is locked to the fundamental using the Hänsch-Couillaud technique, subsequently the second harmonic is also made resonant by slightly rotating the plates. This is achieved by a feedback signal applied to the galvos. The feedback signal is obtained by monitoring the

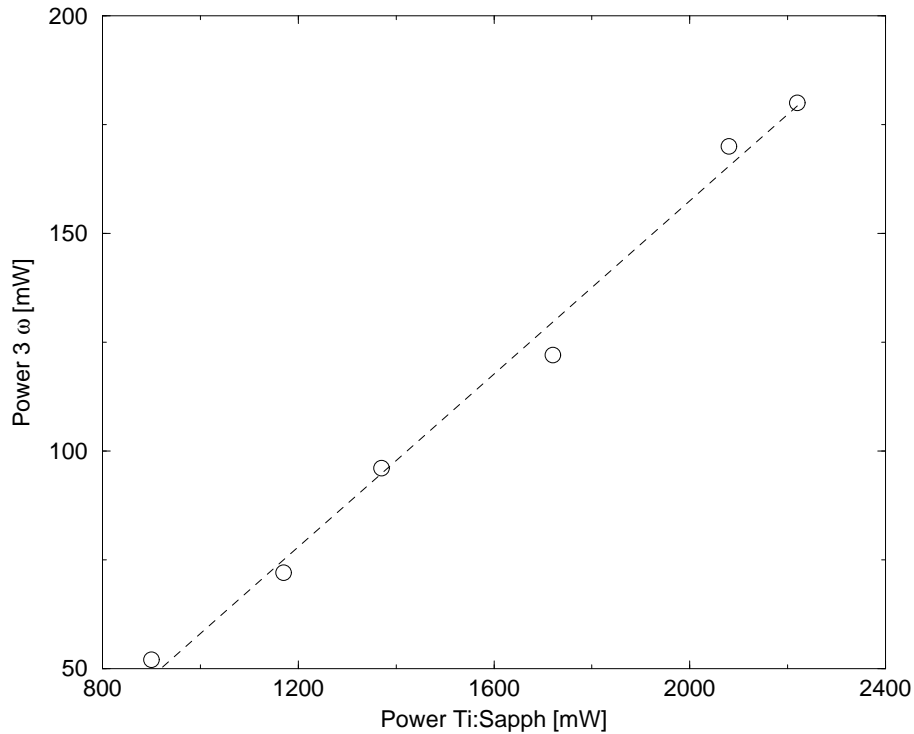


Figure 4.3: Output power of the 3rd harmonic as function of Ti:S power.

rejected 408 nm light from M6. The galvo lock consists of a lock-in amplifier, used at a slow modulation frequency (80Hz) with an additional DC current source added to find the closest resonance for the second harmonic. Fast disturbances (which are experienced by both wavelengths) are compensated by the fast Hänsch-Couillaud lock regulating the piezo, while the slowly varying dispersion is compensated by the galvo plates. The resulting third harmonic output as a function of Ti:S power is shown in figure 4.3.

The deep UV light can be continuously scanned over 10 GHz at 272 nm. With the present optics set the system can generate wavelengths in the range 280 nm to 265 nm. Using other sets of optics and crystals the entire Ti:S range can in principle be frequency tripled, generating wavelengths ranging from 235 nm up to 330 nm. Over many hours of operation, the output power of the system remains constant, implying the optics and BBO crystal are not degrading due to influence of the generated UV light.

4.3 Conclusion

In summary, we have developed an efficient method to generate third harmonic light of any cw single mode laser. An external enhancement cavity is used to generate the second harmonic. A second high finesse enhancement cavity with dispersion compensating elements, enabling the locking of both the fundamental and the second harmonic light of a Ti:S laser simultaneously, generates deep UV. Starting with 2.1 W light at the fundamental wavelength $\lambda = 817$ nm up to 175 mW of output power at 272 nm has been attained. The overall conversion efficiency of the process is 8%. To our knowledge such high output power has never before been achieved using a single tunable laser system.

The authors acknowledge financial supported from the organisation TNO-FEL, the Hague.

Bibliography

- [1] B. Couillaud, L.A. Bloomfield and T.W. Hänsch, *Opt. Lett.* **8**, 259 (1983).
- [2] B. Couillaud, T.W. Hänsch and S.G. McLean, *Opt. Comm.* **50**, 127 (1984).
- [3] S. Bourzeix, B. de Beauvoir, F. Nez, F. de Tomasi, L. Julien F. Biraben, *Opt. Comm.* **133**, 239 (1997).
- [4] S. Sayama and M. Ohtsu, *Opt. Comm.* **137**, 295 (1997).
- [5] Y. Kaneda and S. Kubota, *Opt. Lett.* **20 21**, 2204 (1995).
- [6] T. Fujii, H. Kumagai, K. Midorikawa and M. Obara, *Opt. Lett.* **25 19**, 1457 (2000).
- [7] S. Sayama and M. Ohtsu, *Opt. Comm.* **145**, 95 (1998). (1968).
- [8] T.W. Hänsch, B. Couillaud, *Optics Commun.*, **35**, 441 (1980).
- [9] E. Jurdik, J. Hohlfeld, A.F. van Etteger, A.J. Toonen, W.L. Meerts, H. van Kempen and Th. Rasing, *JOSA B*, **19**, 1660 (2002).
- [10] Z.Y. Ou, S.F. Pereira, E.S. Polzik, and H.J. Kimble, *Opt. Lett.*, **17**, 640 (1992).

Chapter 5

High-resolution spectroscopy on ground-state transitions of samarium-I

A high resolution laser-induced fluorescence study has been performed on thirteen ground-state transitions in Samarium, using a frequency-doubled Ti:Sapphire laser in the wavelength range 350 - 450 nm. From each spectrum isotope shifts and hyperfine structure constants A and B are derived. The results are used to determine the nuclear parameter $\lambda^{AA'}$.

5.1 Introduction

Samarium (Sm) is a rare-earth element with seven stable isotopes with the following abundancies: ^{144}Sm 3.07%, ^{147}Sm 14.99%, ^{148}Sm 11.24%, ^{149}Sm 13.82%, ^{150}Sm 7.38%, ^{152}Sm 26.75% and ^{154}Sm 22.75%. Of these isotopes, ^{144}Sm and ^{152}Sm have recently obtained special interest in the field of cancer treatment. These isotopes become short lived radio isotopes ^{145}Sm and ^{153}Sm , after neutron absorption in a high flux reactor. The isotope ^{145}Sm has its application for brain tumor brachytherapy. The isotope ^{153}Sm is used for treatment of ocular cancer and for pain relief of bone cancer. Since there is not a simple method to enrich these isotopes using conventional techniques, e.g., ultra-centrifuges and calutrons, research towards a suitable spectroscopic route as the basis for laser isotope separation is of great interest.

In the past, spectra of Sm have been studied in detail in the 550 to 650 nm wavelength range [1, 2, 3] using dye- and diode-lasers. This has resulted in a wealth of accurate values of isotope shifts and hyperfine constants for the odd isotopes. However, not so much is known about the higher lying states around 25000 cm^{-1} for which UV light around 400 nm is required. In this energy region dye lasers are difficult to operate, but with the advent of powerful narrow-band

frequency-doubled Ti:Sapphire lasers this region has recently opened up.

We have performed high-resolution laser induced fluorescence experiments on ground-state transitions of Sm. To this end, a continuous-wave frequency-doubled Ti:Sapphire laser was used covering a wavelength range between 350 and 450 nm. Thirteen transitions have been investigated, yielding isotope shift (IS) values, magnetic dipole constants A , and electric quadrupole constants B . From a King plot [8] analysis the nuclear parameter $\lambda^{AA'}$ (related to the change in mean square nuclear radii) is obtained for the various isotopes.

5.2 Experimental setup

The experimental setup is schematically depicted in figure 5.1. Using this setup laser-induced fluorescence (LIF) of Sm in the wavelength range from 350 nm up to 450 nm has been investigated. The light is generated by frequency doubling a narrow-band tunable cw Ti:S laser (Coherent 899-21). The Ti:S laser is pumped by a 10 W Nd:YVO₄ laser at 532 nm (Spectra Physics Millennia-Xs). The output of the Ti:S laser is coupled into a bowtie-shaped external enhancement cavity (EEC). This cavity contains a Brewster-cut nonlinear crystal for frequency doubling. The wavelength range of the EEC is limited by the phase-matching angle of the crystal and by the reflectance of the mirrors of the EEC. To cover the entire wavelength range of the Ti:S laser (700 - 900 nm), three LBO crystals are needed each cut at a different phase-matching angle. In figure 5.2 the second harmonic output power of the EEC using an input power at the fundamental wavelength of 1.00 W, is plotted as a function of the wavelength for one of the LBO crystals used. This crystal is cut at angles of $\theta = 90^\circ$, $\phi = 33.7^\circ$ with respect to the optical axis and has a center wavelength of 780 nm. The other two LBO crystals used in the experiment are cut at $\theta = 90^\circ$, $\phi = 37.8^\circ$ and $\theta = 90^\circ$, $\phi = 27.0^\circ$ respectively. Their center wavelengths are 744 nm and 850 nm, respectively. Mode matching of the Ti:S light into the EEC is performed by a thin lens L1. The cavity losses per round-trip are close to 1%, therefore the reflectivity of the input coupling mirror (M1) is chosen to be 99% to ensure impedance matching. This leads to a maximum coupling of 88% of the fundamental light into the EEC. The mirrors M3 and M4 have a reflectivity $> 99.8\%$ and a radius of curvature of -75 mm to focus the beam in the LBO crystal.

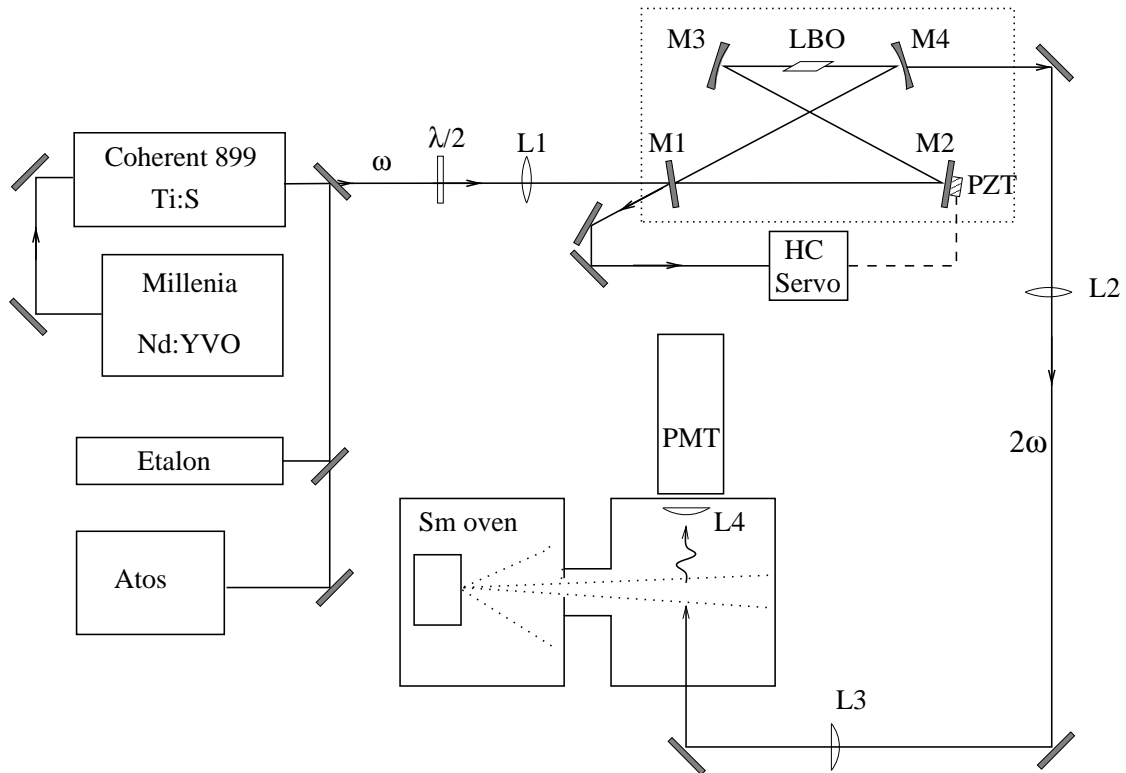


Figure 5.1: *Experimental setup for the Sm laser-induced fluorescence experiment. L1: thin mode-matched lens. M1 - M4: mirrors of external enhancement cavity, PZT: piezo-electric transducer for cavity locking, HC: Hänsch-Couillaud locking set up, L2 - L4: imaging lenses. The wavelength of the Ti:S laser is measured using a wavelength meter (Atos) and an etalon.*

The distance between M3 and M4 is optimized for maximum conversion efficiency. To keep the EEC in resonance, the cavity is locked to the fundamental wavelength using the Hänsch-Couillaud locking technique [5] which supplies a feedback signal to the small ($\varnothing 6$ mm x 2 mm) mirror M2 mounted on a piezo-electric transducer. The second harmonic light is coupled out through M4 which is highly transparent ($> 97\%$) for the wavelengths 350 nm to 450 nm. From the full-width half-maximum of the cavity etalon peaks and the free spectral range a cavity finesse of about 310 is deduced. This leads to a cavity enhancement factor of 98. The bandwidth of the generated light is $\Gamma \lesssim 2$ MHz.

Since the transition $J = 0 \rightarrow J = 1$ at 26281.09 cm^{-1} of Sm has a coincidental overlap with an O_2 absorption, the Ti:S laser and frequency doubling cavity are flushed with N_2 to ensure stable and mode-hop-free operation. During the spectroscopic experiment the absolute wavelength is measured using an ATOS wavemeter LM007, which has a short-term accuracy of 10^{-5} nm ($\approx 5 \text{ MHz}$ at 800

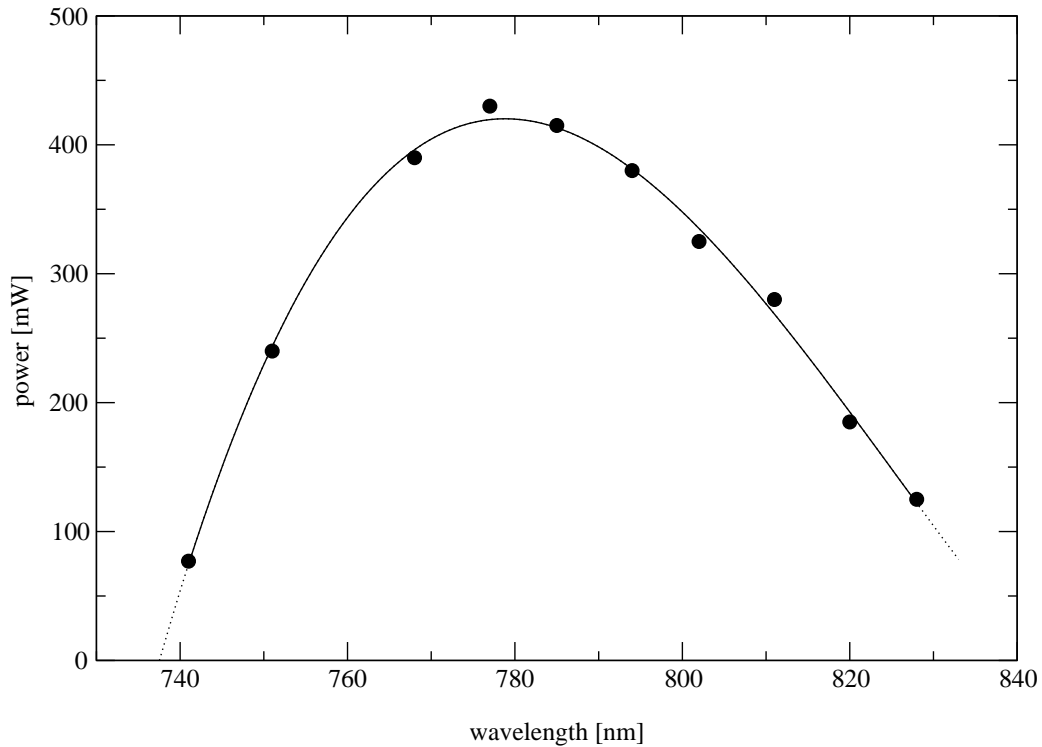


Figure 5.2: Output power of the SHG set-up vs. wavelength using the LBO crystal cut at $\theta = 90^\circ$, $\phi = 33.7^\circ$. The fundamental power is 1 Watt.

nm). A confocal etalon (FSR = 300 MHz and finesse ≈ 100) is used for a relative wavelength calibration.

A beam of Sm atoms is produced under vacuum conditions using a tantalum oven. This oven is heated by electron bombardment using a hot tungsten wire, through which a large current (typically 25V / 30A) is run. Emitted electrons are accelerated towards the oven by an electric field of typically 2 kV/cm. Due to this electron bombardment the tantalum oven heats up to temperatures of about 1200 Kelvin. At this temperature a sufficiently dense atomic beam of Sm is produced. The atoms leave the oven through a small hole of 1.0 mm diameter. The laser beam intersects the atomic beam at a right angle some 60 cm downstream from the oven. Diafrags are used in the atomic beam to reduce the Doppler broadening to ≈ 20 MHz. The background pressure in the vacuum system is about 5×10^{-7} mbar. The LIF light is imaged on a photomultiplier (PMT) sensitive in the UV, which is placed above the intersection region of atomic beam and laser beam.

5.3 Measurements

5.3.1 hyperfine structure

We have measured all known groundstate-transitions of Sm in the energy range of 22000 cm^{-1} to 29000 cm^{-1} . The even isotopes of Sm have no nuclear spin ($I = 0$), therefore the angular momentum J is the relevant quantum number. For the groundstate of Sm $J = 0$. The selection rules for optical transitions are $\Delta J = 0 \pm 1$, and $J = 0 \not\leftrightarrow J = 0$. Hence, from the ground-state only transitions to excited states with angular momentum $J = 1$ are accessible.

The two odd isotopes of Sm, ^{147}Sm and ^{149}Sm , both have nuclear spin $I = 7/2$. Combined with angular momentum $J = 0$ in the ground-state of Sm only a single hyperfine level $F = 7/2$ results. In the excited state, however, $J = 1$, and the nuclear spin couples to the electron spin giving rise to a hyperfine splitting in three components with $F = 5/2$, $F = 7/2$ and $F = 9/2$ respectively. Therefore each spectrum will show 11 peaks, 5 for the even isotopes and 6 for the two odd isotopes. See upper graph in figure 5.3. In some cases two or more peaks overlap (see lower graph in fig. 5.3). In this case, the assignment of the peaks is more difficult.

The hyperfine shift contains two contributions. The first one results from the interaction of the nuclear magnetic moment μ_I with the magnetic field B_{el} due to the motion of the electrons around the nucleus. The second contribution is the interaction between the nuclear quadrupole moment Q_I and the electric field gradient q produced by the electrons. These contributions give rise to additional terms in the Hamiltonian of the atom

$$H_{hfs} = \mu_I \cdot B_{el} + Q_I \cdot q. \quad (5.1)$$

The contributions to the atomic Hamiltonian are small and the energy contributions can be calculated using first order perturbation theory. This leads to [6, 7]:

$$\Delta E_F(I, J, F) = \frac{A}{2}C + \frac{B}{4} \frac{\frac{3}{2}C(C+1) - 2I(I+1)J(J+1)}{(2I-1)(2J-1)IJ}. \quad (5.2)$$

ΔE_F gives the energy shift of the different hyperfine components of the odd isotope with respect to the centre-of-gravity-position in the spectrum. Here A

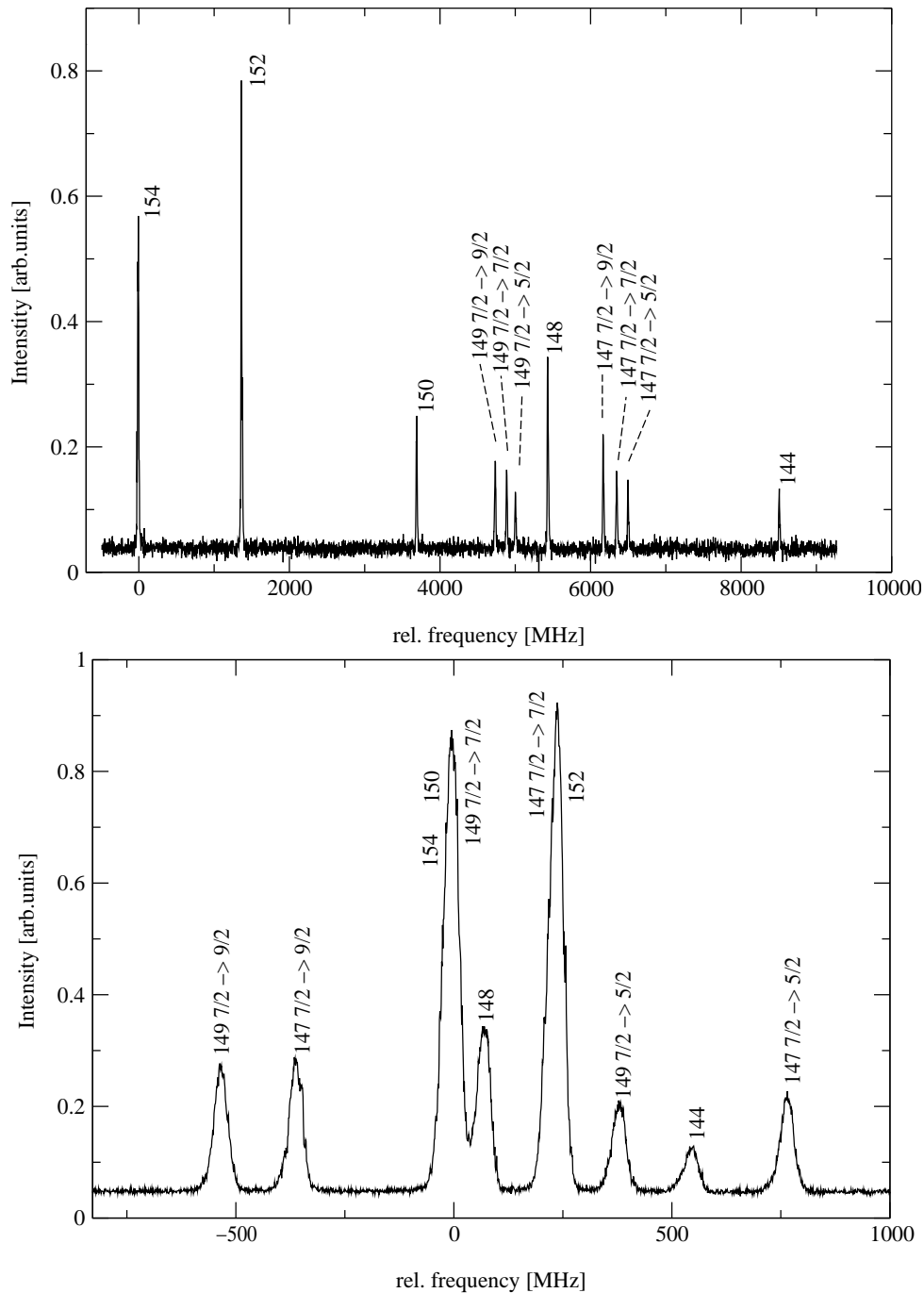


Figure 5.3: *Upper graph: A regular transition at $\lambda = 354.194$ nm, the ordering of the seven isotopes is as expected. Lower graph: The transition at $\lambda = 413.496$ nm. This is a more difficult to assign spectrum, resonances of different isotopes are overlapping and are not ordered "normally". When plotted in a King-plot, a line crossing the zero axis results. Note the different x-axis scale in both graphs.*

is the magnetic dipole coupling constant, B the electric quadrupole coupling

Table 5.1: Observed hyperfine constants A and B (in MHz) for the excited states of Sm as derived from the investigated transitions. For transition (a) at $\lambda = 382.465$ nm, the positions of the odd isotopes could not be determined

| wavelength[nm] | $E[\text{cm}^{-1}]$ | $A(149)$ | $B(149)$ | $A(147)$ | $B(147)$ |
|----------------------|---------------------|-------------|------------|-------------|-----------|
| 354.194 | 28233.1 | -33.41(24) | -0.84(27) | -41.05(3) | 6.5(24) |
| 362.999 | 27548.3 | -100.5(5) | 0.3(27) | -122.4(3) | -2.4(32) |
| 366.731 | 27267.9 | -83.36(8) | 3.8(12) | -100.53(33) | -15.0(13) |
| 370.891 | 26962.1 | 23.92(31) | -2.2(8) | 28.6(5) | 7.81(4) |
| 373.083 | 26803.7 | -307.1(2) | -0.5(12) | -372.8(4) | 0.96(41) |
| 378.240 | 26438.2 | -106.26(1) | -5.8(9) | -128.6(3) | 17.8(17) |
| 380.502 | 26281.1 | -85.5(18) | 11.0(74) | -104.3(6) | -27.2(22) |
| 382.465 ^a | 26146.2 | . | . | . | . |
| 410.246 | 24375.6 | -324.84(35) | 2.1(30) | -394.88(9) | -15.4(4) |
| 413.496 | 24184.0 | -69.5(5) | -9.1(13) | -84.5(3) | 19.5(11) |
| 423.191 | 23623.0 | -31.39(48) | 1.0(7) | -37.6(3) | -9.8(12) |
| 430.222 | 23243.8 | -263.28(5) | 1.72(3) | -319.40(26) | -8.49(8) |
| 436.413 | 22914.1 | -184.4(2) | -10.33(36) | -223.48(4) | 32.6(5) |

constant and C the Casimir factor

$$C = F(F + 1) - I(I + 1) - J(J + 1). \quad (5.3)$$

From the recorded spectra the position of each hyperfine component is determined. From this the centre of gravity of the odd isotope in the excited level can be derived as well as the hyperfine constants A and B . In table 5.1 the constants for all excited levels as deduced from the investigated transitions are collected. An exception is the level at 26146.2 cm^{-1} , where due to overlap with another transition starting from the first excited state at 292.6 cm^{-1} , it was impossible to determine the A and B values.

The ratio between the magnetic dipole constants A_{147}/A_{149} and the electric quadrupole constants B_{147}/B_{149} should be approximately constant for each transition. For Sm $A_{147}/A_{149} \approx 1.2$. However, in all measured transitions the electric quadrupole constants are small, resulting in a relatively large scatter in the ratio B_{147}/B_{149} . It can be seen from eq. 5.4 - 5.6 that for the excited state of Sm in this case, the major contribution in ΔE_F originates from the magnetic dipole interaction and that the electric quadrupole constant has little influence on the

energy shift.

$$\Delta E_F(7/2, 1, 5/2) = -\frac{9A}{2} + \frac{15B}{28}, \quad (5.4)$$

$$\Delta E_F(7/2, 1, 7/2) = -A - \frac{5B}{7}, \quad (5.5)$$

$$\Delta E_F(7/2, 1, 9/2) = -\frac{14A}{4} + \frac{B}{4}. \quad (5.6)$$

5.3.2 Isotope splitting

The observed isotope shifts (IS) in all measured transitions are collected in table 5.2. The IS contains three components: the Normal Mass Shift (NMS), the Specific Mass Shift (SMS) and the Field Shift (FS):

$$\delta\nu_i = \delta\nu_{iNMS} + \delta\nu_{iSMS} + \delta\nu_{iFS}. \quad (5.7)$$

The normal mass shift relates to the change in the reduced mass of electron and nucleus when comparing two isotopes (with mass-numbers A and A' respectively) and can be written as

$$\delta\nu_{iNMS} = M_{iNMS} \frac{A - A'}{AA'}, \quad (5.8)$$

where

$$M_{iNMS} = \frac{\nu_i}{1822.8}. \quad (5.9)$$

Here ν_i is the frequency of the transition. The factor 1822.8 gives the ratio of proton and electron mass. The second term in eq. 5.7 is the specific mass shift which is caused by correlations in the momenta of the electrons. In analogy to 5.8, the specific mass shift can be expressed as

$$\delta\nu_{iSMS} = M_{iSMS} \frac{A - A'}{AA'}. \quad (5.10)$$

The exact value of the SMS is difficult to calculate, since the electronic wavefunctions have to be known. The third term in eq. 5.7 is the field shift, which relates to the changes in the nuclear charge distributions when comparing the

Table 5.2: Observed isotope shifts (MHz) for the measured lines of Sm. The uncertainties are $\leq 0.6\%$. For the transition at $\lambda = 382.465$ nm, the positions of the odd isotopes could not be determined. Their positions have been obtained by interpolation of the King-plot.

| wavelength[nm] | 154 – 152 | 152 – 150 | 150 – 149 | 150 – 148 | 148 – 147 | 148 – 144 |
|----------------------|-----------|-----------|--------------------|-----------|--------------------|-----------|
| 354.194 | –1370.7 | –2328.0 | –1161.4 | –1741.0 | –878.8 | –3074.7 |
| 362.999 | –1141.8 | –1857.7 | –928.0 | –1425.6 | –719.1 | –2552.6 |
| 366.731 | –196.7 | 41.5 | 12.6 | –129.6 | –71.4 | –417.0 |
| 370.891 | 1072.4 | 2408.4 | 1191.1 | 1552.4 | 774.5 | 2437.8 |
| 373.083 | 0.0 | 373.2 | 179.2 | 114.0 | 49.9 | 0.0 |
| 378.240 | –387.8 | –337.0 | –174.6 | –388.3 | –201.4 | –850.1 |
| 380.502 | 816.3 | 1866.3 | 932.7 | 1199.0 | 604.6 | 1863.0 |
| 382.465 ^a | 674.5 | 1269.4 | 625.9 ^a | 886.1 | 436.8 ^a | 1513.1 |
| 410.246 | –147.4 | 147.4 | 58.8 | –69.5 | –33.4 | –307.9 |
| 413.496 | –143.9 | 146.9 | 74.6 | –48.4 | –26.7 | –286.6 |
| 423.191 | –153.1 | 120.4 | 54.7 | –72.1 | –37.7 | –315.9 |
| 430.222 | 1641.7 | 3532.2 | 1747.6 | 2322.2 | 1163.9 | 3724.7 |
| 436.413 | –352.6 | –484.2 | –242.2 | –409.9 | –209.3 | –783.8 |

^a odd isotope positions: interpolation of the King-plot.

various isotopes

$$\delta\nu_{iFS} = E_i f(Z) \lambda^{AA'}. \quad (5.11)$$

Here E_i is a factor related to the electron density at the nucleus, $f(Z)$ is a relativistic correction factor for the field shift. The nuclear parameter $\lambda^{AA'}$ is related to the change in mean-square nuclear charge radii when comparing the isotopes.

In a so called King-plot [8] the measured isotope shifts for transition i are plotted in a particular way against the shifts in a reference transition j . For both transitions the shifts between adjacent isotope pairs are used (eg. the shift between ^{154}Sm and ^{152}Sm). The plot then results in a straight line. When deviations occur, generally this indicates that the peaks in the measured transition have been wrongly assigned. For such a King-plot a reduced isotope shift (RIS) is used, which can be determined by subtracting the NMS from the measured isotope shift and by normalisation of the residual shift with respect to a reference isotope

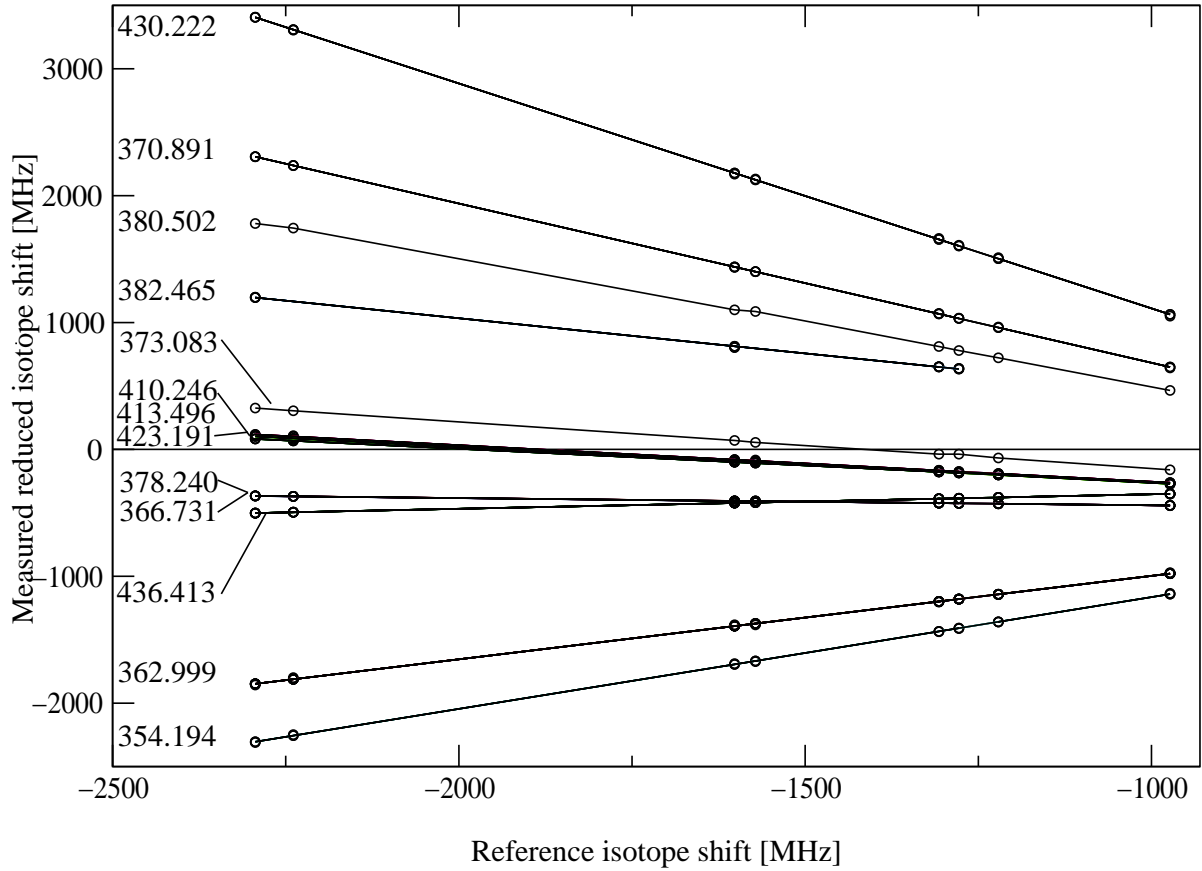


Figure 5.4: King-plot, the obtained reduced isotope shifts are plotted against the reduced isotope shift of a transition at 636.74 nm measured by Jin et al.[2] The numbers in the graph are the wavelengths of the transitions in nm.

pair:

$$\delta\nu_{iRIS} = (\delta\nu_i - \delta\nu_{iNMS}) \left(\frac{AA'}{A - A'} \right) \left(\frac{A_{ref} - A'_{ref}}{A_{ref}A'_{ref}} \right). \quad (5.12)$$

For the following analyses the isotope pair ^{154}Sm - ^{152}Sm is used as reference pair, hence,

$$\delta\nu_{iRIS} = (\delta\nu_{iSMS} + E_i f(Z)\lambda) \left(\frac{AA'}{A - A'} \right) \left(\frac{2}{154 \cdot 152} \right). \quad (5.13)$$

The resulting normalised reduced isotope shift for each measurement i is now plotted against the reduced shifts of a reference line j in a King-plot, see fig. 5.4.

As a reference (x-axis), the measurement of the groundstate $J = 0 \rightarrow J = 1$, $4f^66s^2 \rightarrow 4f^66s6p$ transition at 636.74 nm by Jin et al. [2] was used. This

transition has a large IS, the transition is nearly pure ($ns^2 - nsnp$), hence, the wavefunction has a relatively small admixture of other configurations. The lines in the King-plot can be represented by

$$\delta\nu_{iRIS} = \frac{E_i}{E_j}\delta\nu_{jRIS} + (M_{iSMS} - \frac{E_i}{E_j}M_{jSMS})\frac{2}{154\cdot 152}. \quad (5.14)$$

The slope of the lines in the plot then gives E_i/E_j . Since E_j of the reference transition is known, E_i can be determined. The intercept of the lines with the vertical axis in the plot is

$$(M_{iSMS} - \frac{E_i}{E_j}M_{jSMS})\frac{2}{154\cdot 152}. \quad (5.15)$$

Since the reference transition is nearly pure $ns^2 - nsnp$, the M_{jSMS} factor of this transition is assumed to be zero, according to the semi-empirical relation [14]

$$\delta\nu_{iSMS} \cong (0 \pm 0.5)\nu_{iNMS}. \quad (5.16)$$

Therefore the intercept of the King-plot gives the value of $M_{iSMS}(\frac{2}{154\cdot 152})$. From the value of this intercept $\delta\nu_{iSMS}$ then can be derived. From the observed isotope shift $\delta\nu_i$ and the also known $\delta\nu_{iNMS}$, the field shift for each isotope pair can be extracted. From the FS the values of the nuclear parameter $\lambda^{AA'}$ can be calculated using relation 5.11. The electronic factor E_i is determined from the King-plot. Brand et al. [10] derived that E_j has a value of -0.285 (with an uncertainty of 4%) for the $4f^6s^2 - 4f^66s6p$ transition of Sm I. The factor $f(Z)$ has a value of 20.3 GHz/fm² for a uniformly charged sphere, according to Babushkin [11]. In table 5.3 the values of E_i/E_j , M_{iNMS} , M_{iSMS} and $F = E_i f(Z)$ as derived from King-plots are collected.

5.4 Discussion

The results of the King-plot analyses are collected in the tables 5.3 and 5.4. From the King-plot (fig. 5.4) some further qualitative conclusions can be drawn. The slope of the lines, which varies from positive to negative, is determined by the ratio E_i/E_j (see eq. 5.14), so all overlapping lines have similar electronic structure in the excited state (since they all connect to the same ground-state).

Table 5.3: Values of E_i/E_j , M_{iNMS} , M_{iSMS} and $F = E_i f(Z)$ derived from King-plots. ($E_j = 0.285(\pm 4\%)$ and $f(Z) = 20.3 \text{ GHz}/\text{fm}^2$)

| wavel.[nm] | E [cm ⁻¹] | E_i/E_j | $M_{iSMS}[\text{THz}]$ | $M_{iNMS}[\text{THz}]$ | F |
|------------|-----------------------|--------------|------------------------|------------------------|-------------|
| 354.194 | 28233.1 | 0.878 (6) | -3.37 (18) | 464.92 | 5.08 (20) |
| 362.999 | 27548.3 | 0.655 (11) | -4.25 (22) | 453.39 | 3.79 (12) |
| 366.731 | 27267.9 | -0.0568 (19) | -5.86 (32) | 448.82 | -0.329 (18) |
| 370.891 | 26962.1 | -1.2526 (29) | -6.64 (36) | 444.82 | -7.25 (29) |
| 373.083 | 26803.7 | -0.364 (5) | -3.37 (18) | 441.24 | -2.11 (10) |
| 378.240 | 26438.2 | -0.0585 (18) | -5.86 (32) | 435.17 | -0.339 (16) |
| 380.502 | 26281.1 | -0.991 (9) | -5.65 (31) | 433.11 | -5.73 (24) |
| 382.465 | 26146.2 | -0.554 (10) | -0.8778 (43) | 430.33 | -3.21 (12) |
| 410.246 | 24375.6 | -0.280 (7) | -6.33 (35) | 401.22 | -1.62 (9) |
| 413.496 | 24184.0 | 0.286 (7) | -6.31 (35) | 398.02 | 1.65 (9) |
| 423.191 | 23623.0 | -0.2623 (14) | -6.07 (31) | 389.08 | -1.52 (6) |
| 430.222 | 23243.8 | -1.77 (6) | -7.62 (42) | 382.57 | -10.24 (51) |
| 436.413 | 22914.1 | 0.1152 (10) | -2.78 (15) | 377.14 | 0.667 (26) |

Table 5.4: Average values of the nuclear parameter $\lambda^{AA'}$ calculated from our experiments and the values obtained in electron-scattering experiments from ref. [13]. The error is mainly determined by the uncertainty in E_j and $f(Z)$.

| AA' | $\lambda^{AA'}[\text{fm}^2]$ | $\lambda^{AA'}[\text{fm}^2]\text{ref.}[13]$ |
|---------|------------------------------|---|
| 154-152 | 0.220 (14) | 0.221 (14) |
| 152-150 | 0.407 (27) | 0.411(27) |
| 150-149 | 0.202 (12) | 0.224 (12) |
| 150-148 | 0.291 (15) | 0.303 (15) |
| 148-147 | 0.147 (8) | 0.171 (8) |
| 148-144 | 0.497 (24) | 0.478 (24) |

In Sm under study, two electronic configurations are relevant and may be mixed in the excited states: $4f^6.6s.np$ and $4f^5.5d.6s^2$. In a King-plot with as reference a pure $4f^6.6s^2 \rightarrow 4f^6.6s.6p$ transition, a positive slope indicates a dominant $4f^5.[6F].5d.6s^2.7F$ character of the excited state, whereas the negative slope must be attributed to more dominant contributions of the $4f^5.[6F].5d.6s^2.7F$ configuration. This is confirmed by the information on the atomic spectra database

of the NIST [9], indicating that the excited states involved in the transitions at 380.502 nm and 430.222 nm have respectively a dominant $4f^5.[6F].5d.6s^2.7F$ and $4f^5.[6F].5d.6s^2.7G$ character (see fig.5.4). Without quantitative information on the value of E_i for a pure $4f^5.5d.6s^2$ configuration it is not possible to analyse the slopes of the King-plot in more detail.

For the observed transition at $\lambda=382.465$ nm (level at 26146.0 cm^{-1}) the odd isotopes could not be assigned since the spectrum shows many weak lines. This is due to overlap with a transition starting from the first metastable state at 292.58 cm^{-1} to the $4f^5(6F)5d.6s^2.9H$ level at 26438.25cm^{-1} . The positions of the odd isotopes are determined by interpolation of the King-plot. One transition reported in literature (at 26910 cm^{-1} [9]) could not be observed in our experiment, even at very high atom density.

Regarding the nuclear parameter, it could be argued that the exact value of the SMS of the reference transition is an approximation. It would make more sense to use the $\lambda^{AA'}$ data from electronic scattering experiments [13] to determine the FS and obtain in this way information on the value of the SMS. Blaum et al.[12] used this approach to test the approximation $\delta\nu_{iSMS} \cong (0 \pm 0.5)\delta\nu_{iNMS}$ for a pure $ns^2 - nsnp$ transition in case of Gadolinium. It turned out that for their case the approximation $\delta\nu_{iSMS} \cong 0$ was not really correct. We have also tested this approach here. However, the electronic scattering experiments on Sm yield values of $\lambda^{AA'}$ with large uncertainties. Extrapolation of the lines in a King-plot based on these data to determine the intercept would not yield more precise values for the SMS.

5.5 Conclusion

We have reported on high resolution measurement of Sm-I transitions from the $J = 0$ ground-state to $J = 1$ excited states in the 23000 cm^{-1} - 29000 cm^{-1} energy range. One reported line (at 26910cm^{-1} [9]) could not be observed in our experiment even at high atom density. The values of the nuclear parameter $\lambda^{AA'}$, obtained from our measurements agree with the results from Jin et al. [2] and the data from muonic and electron scattering experiments [13].

The authors acknowledge financial support from the organisation TNO-FEL, the Hague.

Bibliography

- [1] J.A.R. Griffith, G.R. Isaak, R. New, M.P. Ralls, C.P. van Zyl, *J. Phys. B: At. Mol. Phys.* **12**, L1, (1979).
- [2] W.G. Jin, T. Horiguchi, W. Yang and I. Endo, *Phys. Rev. A* **49** 6 (1994) 4398.
- [3] T. Kobayashi, I. Endo, A. Fukumi, T. Horiguchi, Y. Ishida, T. Kondo, T. Kuwamoto, N. Mimamoto, T. Nakamura, T. Takahashi, *Zeitschrift fuer Physik D.* **39**, 209 (1997).
- [4] A. Fukumi, I. Endo, *Zeitschr. fuer Phys D.* **42** 243-249 (1997).
- [5] T.W. Hänsch, B. Couillaud, *Optics Commun.*, **35**, 441 (1980).
- [6] H. Kopfermann, *Nuclear moments* (Academic Press, New York, 1958).
- [7] G.K. Woodgate, *Elementary Atomic Structure 2nd ed.* (Oxford University Press, Oxford, 1989).
- [8] W.H. King, *Isotope Shifts in Atomic Spectra*, Plenum Press, New York/London (1984).
- [9] Atomic-Spectra-Data-Base on website of NIST. Address: <http://physics.nist.gov/PhysRefData/contents-atomic.html>
- [10] H. Brand, B. Seibert and A. Steudel, *Zeitschrift fuer Physik A* **296** 281-286 (1980).
- [11] R. Babushkin, *Phys. Rev.* **188** (1969) 1916.
- [12] K. Blaum, B.A. Bushaw, S. Diel, Ch. Geppert, A. Kuschnick, P. Müller, W. Nörtershäuser, A. Schmitt and K. Wendt, *Eur. Phys. J. D.* **11** 37-44, (2000).
- [13] G. Fricke, C. Bernardt, K. Heilig, L.A. Schaller, L. Schellenberg, E.B. Shera, C.W. De Jager, *At. Data Nucl. Data Tables* **60** 117, (1995).
- [14] K. Heilig and A. Steudel: *At. Data Nucl. Data tables* **14** (1974) 613.
- [15] E.C. Setzer, *Phys. Rev.* **188** (1969) 1916.

Summary

This thesis comprises an experimental study on optical parametric oscillators (OPO), sum-frequency mixing devices and their spectroscopic applications.

These non-linear optical devices are sources of coherent radiation and can be used to extend the wavelength range of existing lasers. In general, they are composed of a non-linear crystal inside an optical resonator. Inside the crystal an applied optical field (a beam of laser light) induces polarisation effects; the molecular dipoles in the crystal will start to oscillate at the same frequency as the applied field. This dipole oscillation in turn leads to the emission of an electro-magnetic (EM) wave at the same frequency as the applied EM field. When the incident light field is sufficiently strong, non-linear effects occur; *i.e.* the dipole-oscillation is no longer harmonic, but will contain an-harmonic terms. Hence, this polarisation will generate an EM field that corresponds to these an-harmonic terms, resulting in light at other frequencies.

In an OPO a powerful laser-beam (the pump) is converted into two new wavelengths (the signal and idler wave) while conserving energy and momentum. Frequency mixing, on the other hand, is the opposite process; two wavelengths are combined in a non-linear medium to generate the sum or the difference of the frequencies of the incident waves, again conserving momentum and energy. By "adding up" two photons, higher energy photons can be generated, *viz.* sum-frequency mixing can be used to generate ultra-violet light from visible light. Difference-frequency mixing can be used to produce infra-red light, as low energy photons are generated. These techniques can be applied to generate coherent light in a broad range of wavelengths in the electro-magnetic spectrum. Using solid state lasers in combination with non-linear techniques radiation in a large wavelength range, starting from 200 nm up to 5 μm , can be generated.

The application of these non-linear optical systems depends strongly on the output characteristics of the generated radiation, such as wavelength, pulse-length and bandwidth. For spectroscopic and many other applications often a narrow-bandwidth is desirable. This thesis is focused on the generation of narrow-bandwidth radiation by both pulsed and continuous-wave devices.

In chapter 2, a tunable single-longitudinal-mode (SLM) OPO system is described, that can be electronically scanned over 2.5 cm^{-1} . To reduce the bandwidth of the OPO system, a configuration with a narrow-bandwidth seed oscillator is used. The narrow-bandwidth seed-oscillator contains a grating at grazing incidence angle for maximum wavelength selectivity. To obtain sufficient power, the output of the seed oscillator is injected in an amplifier, the power OPO. This seeder-amplifier system provides a stable narrow bandwidth output power (about 11 mJ in 1.5 ns pulses when pumped with 355nm pulses from a Nd:YAG laser) with an overall efficiency of 14.5%. This device is demonstrated to be widely applicable in spectroscopy.

In chapter 3 a novel design for a nanosecond OPO is reported. The design involves a ring cavity-configuration with a grazing-incidence grating. This travelling-wave OPO is pumped by the third harmonic of multi-mode as well as single-mode Nd:YAG lasers. The observed bandwidth of 0.5 GHz at a pulse duration of 1.3 ns when pumped with the single-mode laser is close to the Fourier-transform limit. The configuration of a frequency-selective ring cavity is compact and walk-off compensated and exhibits a relatively low threshold. It could serve as a seed-oscillator for a power OPO similar to the system described in chapter 2.

In chapter 4 a new and efficient method to generate the third harmonic of any single continuous-wave (cw) laser is discussed. It is demonstrated in a device to generate tunable UV-radiation by frequency-tripling of a Ti:Sapphire (Ti:S) ring laser. An external cavity locked to the Ti:S is used to enhance the output intensity and to generate the second harmonic. Subsequently, this second harmonic light is coupled into a second enhancement cavity, together with the fundamental light. To fulfil resonance conditions for both waves simultaneously –which is not trivial because of dispersion in the crystal– this cavity is equipped with dispersion compensating elements. By locking both the fundamental and the second harmonic light of the Ti:S laser simultaneously, deep UV-light is generated in a BBO crystal. Up to 175 mW of output power near 272 nm has been produced, starting from 2.1 W light at the fundamental wavelength.

Chapter 5 comprises the application of a second harmonic cavity for spectroscopy on samarium. A high resolution laser-induced fluorescence study has been performed on thirteen ground-state transitions, using a frequency-doubled Ti:S laser in the wavelength range 350 - 450 nm. From each spectrum isotope shifts and

hyperfine structure constants are derived. Analyses of the data on the isotope shifts in King plots result in a determination of the nuclear parameter $\lambda^{AA'}$ (related to the change in mean square nuclear radii) for the various isotopes.

Samenvatting

In dit proefschrift worden enkele optische parametrische oscillatoren (OPO's) en systemen voor het mengen van optische frequenties alsmede enkele spectroscopische toepassingen beschreven.

OPO's en systemen voor optische frequentie menging zijn bronnen van coherent licht, die straling genereren met dezelfde eigenschappen als laserlicht (zoals hoge intensiteit, kleine divergentie) maar in een uitgebreider golflengte gebied dan de meeste lasers.

Deze niet-lineaire optische systemen bestaat over het algemeen uit een dubbelbrekend, niet-lineair kristal in een optische trilholte (bijv. twee evenwijdige hoogreflecterende spiegels). Wanneer een laser bundel het kristal wordt ingestuurd, dan wordt het kristal gepolariseerd; de dipolen van de molekulen waaruit het kristal is opgebouwd zullen oscilleren met de dezelfde frequentie als die van het binnenkomende licht. Deze oscillatie van de dipolen leidt op zijn beurt weer tot het opwekken van een electro-magnetische (em) golf (zoals licht). Het gegenereerde licht zal dezelfde richting en frequentie hebben als het ingestraalde licht. Wanneer het ingestraalde licht echter een hoge intensiteit heeft, kunnen de dipolen niet meer precies de beweging van de aandrijvende oscillatie volgen (anharmonische beweging). Deze resulterende polarisatie zal een em-veld genereren dat overeenkomt met de anharmonische termen en zal dus andere frequenties produceren. Op deze wijze kunnen andere kleuren licht worden gegenereerd.

In een OPO wordt een intense, monochromatische laserbundel (de "pomp" bundel) via het bovenstaande principe omgezet in twee nieuwe golflengten; de "signaal- en de idler-golven. Hierbij geldt impuls en energie behoud voor de betrokken fotonen. Bij frequentie menging gebeurt het omgekeerde; twee invallende fotonen worden gekombineerd, waarbij een foton met de verschil- of som-frequentie wordt gegenereerd. Door de energie van twee fotonen op te tellen –som-frequentie menging– worden fotonen van hoge energie gemaakt, zoals bijvoorbeeld ultraviolet licht. Ook kan de verschil-frequentie van twee kleuren licht gemaakt worden, waarbij fotonen met een lage frequentie zoals infra-rood licht, gegenereerd

worden.

De toepasbaarheid van deze lichtbronnen is sterk afhankelijk van de eigenschappen (bijv. pulslengte, intensiteit en bandbreedte) van het gegenereerde licht. Voor spectroscopische toepassingen is met name de frequentie bandbreedte erg belangrijk. Dit proefschrift concentreert zich op smalbandige stralingsbronnen van zowel gepulst als continu coherent licht.

In hoofdstuk 2 van dit proefschrift wordt een smalbandig OPO systeem beschreven dat nanoseconde pulsen geeft. Dit systeem bestaat uit een smalbandige oscillator (giopo) die golflengte en bandbreedte van het systeem bepaald, en een versterker, die het smalbandige licht versterkt. De oscillator bestaat uit twee niet-lineaire Beta-bariumboraat (BBO) kristallen in een trillholte, die gevormd wordt door twee spiegels en een tralie. Door de dispersie op het tralie zal een deel van de gegenereerde licht op de tweede spiegel vallen en terug-reflecteren de trillholte in; deze worden verder versterkt. Kleuren met een afwijkende golflengte zullen door het tralie in een andere richting gereflecteerd worden. Door de hoek tussen het tralie en de tegenoverstaande spiegel te veranderen kan de golflengte van het systeem veranderen.

De versterker (popo) bestaat uit een eenvoudige trillholte; twee vlakke spiegels en een kristal. Hierin wordt het licht van de giopo gekoppeld. Omdat de trillholten van de giopo en de popo in lengte verschillen, zal de popo tevens als golflengtefilter werken en alleen de hoofdmode van de giopo versterken. Eventuele zijmodes uit de giopo passen niet in de trillholte van de popo en worden dus niet versterkt. Het systeem wordt gepompt door de derde harmonische van een gepulste Nd:YAG laser, 1.5 ns en 11 mJ levert. Het giopo-popo systeem levert pulsen van 1.5 ns en 11 mJ en heeft een efficiency van 14.5%.

Hoofdstuk 3 behandelt een smalbandige, gepulste OPO met een ringvormige trillholte. In deze trillholte vormt het licht een lopende golf die rondgaat via een tralie om de bandbreedte te reduceren. De compacte configuratie geeft pulsen van 1.5 ns lengte en een bandbreedte van 500 MHz, bij gebruik van een smalbandige pomplaser die in één enkele longitudinale mode werkt.

In hoofdstuk 4 wordt een nieuwe methode gepresenteerd om de derde harmonische van een continue laser te maken. Deze methode maakt het mogelijk om van

één enkele cw laser efficiënt de derde boventoon te maken. Golflengte verstembbaar ultra-violet licht bij 272 nm is geproduceerd, uitgaande van straling van een titaan-saffier laser bij 816 nm. In een frequentie verdubbelings trilholte met een lithium-boraat (LBO) kristal wordt de tweede harmonische gegenereerd bij 408 nm, vervolgens wordt dit licht samen met het licht van 816 nm in een tweede trilholte gestuurd waar in een BBO kristal in som-frequentie generatie optreedt. De trilholtes moeten worden gestabiliseerd zodat de inkomende lichtgolf er precies inpast. Zodoende kan er door constructieve interferentie een hogere intensiteit worden opgebouwd, wat nodig is voor efficiënte werking van de niet-lineaire kristallen. Een probleem doet zich echter voor in de tweede trilholte waarin twee verschillende golven moeten passen. Op het eerste gezicht zou een golf en de verdubbelde golflengte beide in eenzelfde trilholte moeten passen. Maar door dispersie effecten in het kristal gaan de golven uit fase lopen. Door nu twee glasplaatjes in de trilholte te plaatsen, die kan deze dispersie gecompenseerd worden en kan met hoge efficiëntie de derde harmonische worden gegenereerd. Het systeem produceert uitgaande van 2.1 W rood licht, 175 mW verstembbaar uv-licht van zeer kleine bandbreedte (≤ 3 MHz).

In hoofdstuk 5 is een frequentie verdubbelings trilholte gebruikt voor fluorescentie spectroscopie aan Samarium (Sm). Dertien overgangen vanaf de grondtoestand van Sm zijn gemeten in het golflengte gebied van 350 nm tot 450 nm. Uit de verschillende spectra konden de isotopie verschuivingen en de hyperfijnstructuurconstanten bepaald worden.

Dankwoord

Hierbij wil ik een aantal mensen bedanken voor hun bijdrage aan dit proefschrift. *Wim Hogervorst*, mijn promotor, die er vertrouwen in had om mij als HTS-er aan een promotie onderzoek te laten beginnen. *Eric-Jan van Duijn*, voor dagelijkse begeleiding in het lab en het meedenken met mijn projecten. *Marc Leblans* wil ik bedanken voor de prettige en leerzame samenwerking bij het kwikproject. *Paul Tol*, bedankt voor je hulp en geduld bij alle mogelijke Mathematica problemen. *Alle mensen uit de vakgroep* die een grote of kleine bijdrage hebben geleverd; bedankt voor natuurkundige-, technische-, computer- of andere adviezen of hulp. *Harold Linnartz*, bedankt voor de introductie in de fysica van de ontladings nozzel en de cavity ringdown experimenten, die helaas niet in dit proefschrift zijn opgenomen.

I would like to thank *Vitaly Tugbaev* for the nice experiments we performed together, leading to chapter 3 of this thesis. *Hans*, bedankt voor je hulp met cavity-ringdown experimenten en vooral ook voor allerlei andere gezelligheid. Natuurlijk de gezellige mensen uit de atoomfysica groep waarmee wekelijkse bezoeken aan de Weber en de Bio-bar werden gemaakt; *Stefan, Jeroen, Roland en John*. En niet te vergeten mijn goede vrienden uit de vroegere fysische-chemie groep, *Wim* en *Ole*.

Mijn broer *Mark* wil ik bedanken voor het maken van de kaft van dit proefschrift.

September 2003,

Joop

Publications

The thesis is based on the following scientific publications:

- **Chapter 2**

A SLM optical parametric oscillator for spectroscopic applications

J. Mes, M. Leblans and W. Hogervorst,
Optics Letters **109**, 9772 (2002)

- **Chapter 3**

**Travelling-wave Nanosecond Optical Parametric Oscillator
close to the Fourier-Transform Limit**

J. Mes, W. Hogervorst and V. Tugbaev,
Optics Communications **196**, 229 (2001).

- **Chapter 4**

**Third harmonic generation of a cw Ti:Sapphire laser
in external resonant cavities**

J. Mes, R. Zinkstok, S. Witte, E.J. van Duijn and W. Hogervorst,
Applied Physics Letters **vol. 82 number 25**, 23 juni (2003)

- **Chapter 5**

High resolution spectroscopy on Sm-I

J. Mes, E.J. van Duijn and W. Hogervorst
to be submitted

Further publications to which the author has contributed:

- **Laser-Induced Fluorescence Studies of Excited Sr Reactions. 1. $\text{Sr}(^3\text{P}_1) + \text{HF}$**

J.M. Teule, J. Mes, J. Bulthuis, M. H. M. Janssen and S. Stolte
Journal of Physical Chemistry A **102**, 9482 (1998).

- **Magnetic correlations between Co-modified γ -Fe₂O₃ particles in a solid matrix studied by neutron depolarisation in fields up to 0.5 T**

P.Por, J.Mes, W.Kraan and T. Rekveldt

Journal of Magnetism and Magnetic Materials **155** (1996).

- **Electronic Gas Phase Spectrum of the Pentaacetylene Cation**

P. Cias, O. Vaizert, A. Denisov, J. Mes, H. Linnartz and J.P. Maier

Journal of Physical Chemistry A **106**, 9890 (2002)